Kα-lines of the lower charge states of Argon

Bachelorarbeit aus der Physik

Vorgelet von
Andreas Wolf
am 3. September 2013

Dr. Karl Remeis-Sternwarte Bamberg
Erlangen Centre for Astroparticle Physics
Friedrich-Alexander-Universität Erlangen-Nürnberg

Betreuer: Prof. Dr. Jörn Wilms

Zusammenfassung

In dieser Arbeit werden K-Schalen-Spektren von helium- bis hin zu neonähnlichem Argon behandelt. Die Spektren wurden mit der SuperEBIT Elektronenstrahl-Ionenfalle und dem EBIT Kalorimeter Spektrometer am Lawrence Livermore National Laboratory aufgenommen. Sowohl die zugrunde liegenden Aspekte der Atomphysik als auch der experimentelle Aufbau werden ausführlich behandelt. Eine Simulation der Argonspektren wird mit dem Flexible Atomic Code (FAC) durchgeführt. Durch den Vergleich der gemessenen mit den simulierten Spektren werden die stärksten Kα-Linien – d.h. Übergänge von $n = 2$ nach $n = 1$ – identifiziert. Die gemessenen Übergangsenergien werden mit den theoretischen Werten aus der Berechnung mit FAC verglichen. Auf etwaige Probleme bei der Simulation der Spektren und deren Einfluss auf die Identifikation der Kα-Linien wird eingegangen.

Abstract

In this thesis K-shell spectra of He-like through Ne-like argon measured with the SuperEBIT electron beam ion trap and the EBIT calorimeter spectrometer at the Lawrence Livermore National Laboratory are presented. Both the underlying atomic physics and the experimental setup are discussed in detail. A simulation of the argon spectra is performed with the Flexible Atomic Code (FAC). By comparing the measured and the simulated spectra, the strongest Kα-lines, i.e., transitions from $n = 2$ to $n = 1$, are identified. The measured transition energies are compared with the theoretical values of the calculation with FAC. Problems that occured during the simulation of the spectra and their impact on the line identification are addressed.

Contents

Chapter 1

Introduction

The scientific discipline of spectroscopy was essentially founded by Joseph Fraunhofer (1814). In 1814, he discovered numerous dark lines in the solar spectrum during his study of the dispersion and the refractivity of different types of glass. In a systematic investigation, he measured the distances between these lines with a theodolite. That way, over 570 lines were mapped altogether. By carefully altering his optical setup, Fraunhofer could already rule out that the lines emerge because of optical effects. Hence, he concluded that they are an inherent feature of the solar light. However, a satisfying explanation for the origin of these features could only be given after nearly half a century through the work of Kirchhoff & Bunsen (1861) and Kirchhoff (1860). They used spectral analysis in order to examine the emitted light of heated elements. Next to the discovery of the elements caesium and rubidium, the main finding of their work was a coincidence between some of their measured emission lines with the Fraunhofer lines. Thus, the cause of the Fraunhofer lines was correctly deduced to be the absorption and isotropic re-emission of light in the Sun's outer regions. Additionally, first clues about the composition of the Sun's atmosphere could be gathered.

From that time onwards, spectroscopy provided the main way to investigate astronomical objects. Today, various parameters, such as the luminosity, the density, and the temperature of these objects, can very well be estimated through fitting their spectra (Beiersdorfer et al., 2012). In the X-ray regime, present-day spectra are acquired with several X-ray observatories, e.g. Chandra and XMM-Newton. However, in order to extract the entire information of their measured data, very accurate results from atomic physics about the specific energy levels of most elements are required. A prime example of this is the need of rest wavelengths for the determination of the radial speed of celestial objects via the Doppler effect (Doppler, 1842). Based on the fundamental importance of these reference data, various atomic codes for the calculation of wavelengths have been written, alongside laboratory measurements (Beiersdorfer et al., 2012).

In this thesis, measurements of argon K-shell transitions of several charge states produced in an electron beam ion trap are analyzed. Chapter 2 gives a short introduction to the underlying aspects of atomic physics. It explains the calculation of energy levels in quantum mechanics – with particular emphasis on the approximations used for many-electron atoms or ions – and the radiative processes that lead to the emergence of spectra. Following an overview of the measurement with the electron beam ion trap, the detector is calibrated and some of its features are closely looked at in chapter 3. This chapter closes with the identification of the Kα-lines and a comparison to the results of an atomic code. Finally, chapter 4 gives a short summary of the obtained results, alongside the discussion of smaller problems and an outlook on possible experiments to come.

Chapter 2

Atomic Physics

Since it is the most famous problem in atomic physics and actually one of the few solvable ones, we will start our crash course with the simplest of all atoms, that is to say the hydrogen atom. While mainly handling many-electron atoms in this work, the better part of the concepts treated here, such as the splitting of energy levels, the interaction of atoms with electromagnetic radiation, and the emergence of spectra can easily be transfered to more complex systems. The definitions and derivations in the following sections follow the style of Bransden & Joachain (2003) and Shankar (1994).

2.1 The Hydrogen Atom

The hydrogen atom is a two-body problem consisting of an electron of charge $-e$, mass m, and position $\mathbf{r}_e$, which is interacting with a proton of charge e, mass M, and position $\mathbf{r}_p$. The interaction is described by the Coulomb potential

$$V = -\frac{e^2}{4\pi\epsilon_0 \left|\mathbf{r}_e - \mathbf{r}_p\right|}. \tag{2.1}$$

By working in the center of mass (CM) frame with the relative coordinate $\mathbf{r} = \mathbf{r}_e - \mathbf{r}_p$, the relative motion of the electron and the proton can be separated from the CM motion (Shankar, 1994). The latter matches the motion of a free particle, so that the two-body problem is effectively reduced to a one-body problem of a particle with the reduced mass

$$\mu = \frac{mM}{m + M}. \tag{2.2}$$

In spherical coordinates the Laplace operator is given by

$$\Delta = \frac{\mathrm{d}^2}{\mathrm{d}r^2} + \frac{2}{r}\frac{\mathrm{d}}{\mathrm{d}r} - \frac{L^2}{\hbar^2 r^2} \tag{2.3}$$

where

$$\mathbf{L} = \mathbf{r} \times \mathbf{p} \tag{2.4}$$

is the angular momentum operator with $\mathbf{p}$ the momentum operator. The hydrogen atom's energy levels and wave functions are determined by solving the Schrödinger equation

$$\underbrace{\left[-\frac{\hbar^2}{2\mu}\left(\frac{\mathrm{d}^2}{\mathrm{d}r^2} + \frac{2}{r}\frac{\mathrm{d}}{\mathrm{d}r}\right) + \frac{L^2}{2\mu r^2} + V(r)\right]}_{=:H}\Psi_E = E\Psi_E. \tag{2.5}$$

Since the Coulomb potential and consequently equation (2.5) is invariant under spatial rotations, the Hamiltonian H can be diagonalized simultaneously with the squared angular momentum operator L^2 and one of the components of L, which we choose to be L_z. The eigenfunctions of L^2 and L_z are given by the spherical harmonics Y_{lm} (Shankar, 1994). They fulfill the eigenvalue equations

$$L^2 Y_{lm} = \hbar^2 l(l+1) \tag{2.6}$$

$$L_z Y_{lm} = \hbar m \tag{2.7}$$

where $l \in \mathbb{N}$ denotes the orbital angular momentum quantum number and $m \in \{-l, -l+1, ..., l\}$ the magnetic quantum number[1]. Since all terms of the Hamiltonian other than L^2 act solely on the radial component r, the eigenfunctions of equation (2.5) can be rewritten as (Shankar, 1994)

$$\Psi_{Elm}(r, \Theta, \Phi) = R_{El}(r)Y_{lm}(\Theta, \Phi) =: \frac{U_{El}(r)}{r}Y_{lm}(\Theta, \Phi) \tag{2.8}$$

The Schrödinger equation then simplifies to

$$\left[-\frac{\hbar^2}{2\mu}\frac{\mathrm{d}^2}{\mathrm{d}r^2} + \frac{\hbar^2 l(l+1)}{2\mu r^2} + V(r) \right] U_{El}(r) = EU_{El}(r). \tag{2.9}$$

Note that the subscript of the quantum number m has been dropped. Due to spherical symmetry, the choice of the z-axis is downright arbitrary. Hence neither the Schrödinger equation nor the radial part of the eigenfunctions depend on the quantum number m and every energy level will be $(2l+1)$-fold degenerate (Bransden & Joachain, 2003). In order to solve equation (2.9), it is convenient to first consider the asymptotic limits (Shankar, 1994). In order to obtain normalizable eigenfunctions, one has to require

$$U_{El} \xrightarrow[r \to \infty]{} 0. \tag{2.10}$$

Thus at large r equation (2.9) becomes

$$-\frac{\hbar^2}{2\mu}\frac{\mathrm{d}^2 U_{El}}{\mathrm{d}r^2} = EU_{El} \tag{2.11}$$

and has the normalizable solution

$$U_{El}(r) = \exp(-\kappa r) \text{ with } \kappa = \frac{1}{\hbar}\sqrt{-2\mu E}. \tag{2.12}$$

Furthermore, we want the whole expression in the square brackets in equation (2.9) to be a Hermitian operator with respect to its eigenfunctions. It can be shown (Shankar, 1994) that this requirement is equivalent to:

$$\left(U_1^* \frac{\mathrm{d}U_2}{\mathrm{d}r} - U_2\frac{\mathrm{d}U_1^*}{\mathrm{d}r} \right)\Big|_0^\infty = 0. \tag{2.13}$$

Here, U_1 and U_2 represent any two of the radial functions introduced in equation (2.8). At the upper limit the term vanishes due to (2.10), whereas the lower limit is zero if

$$U_{El} \xrightarrow[r \to 0]{} c \tag{2.14}$$

with c a constant. However, for $c \neq 0$ Ψ_{E00} will not solve the Schrödinger equation at the origin (Shankar, 1994) because

$$\Delta(1/r) = -4\pi\delta^3(r). \tag{2.15}$$

With the centrifugal barrier dominating the Coulomb potential for $r \to 0$, equation (2.9) is reducible to

$$\frac{\hbar^2}{2\mu}\frac{\mathrm{d}^2 U_{El}}{\mathrm{d}r^2} = \frac{\hbar^2}{2\mu r^2}l(l+1)U_{El}. \tag{2.16}$$

The ansatz $U_{El} \propto r^\alpha$ then yields

$$\alpha(\alpha - 1) = l(l+1) \tag{2.17}$$

and

$$\alpha = l+1 \text{ or } \alpha = -l \tag{2.18}$$

where only the first solution satisfies (2.14) for $c = 0$. After rescaling $\rho = \kappa r$, equation (2.9) becomes

$$\left[\frac{\mathrm{d}^2}{\mathrm{d}\rho^2} - \frac{l(l+1)}{\rho^2} + \frac{\rho_0}{\rho} - 1 \right] U_{El}(\rho) = 0 \tag{2.19}$$

---

[1]It should be evident out of context whether m denotes the electron's mass or the magnetic quantum number.

with

$$\rho_0 = \frac{\mu e^2}{2\hbar^2 \pi \epsilon_0 \kappa}. \tag{2.20}$$

Applying the asymptotic limits (2.10) and (2.14), the general solution can be written as

$$U_{El}(\rho) = \rho^{l+1} \exp(-\rho) w(\rho) \tag{2.21}$$

and one obtains the following differential equation for $w(\rho)$:

$$\left[\rho \frac{\mathrm{d}^2}{\mathrm{d}\rho^2} + 2(l + 1 - \rho)\frac{\mathrm{d}}{\mathrm{d}\rho} + (\rho_0 - 2(l + 1)) \right] w(\rho) = 0. \tag{2.22}$$

The ansatz of a power series, i.e.,

$$w(\rho) = \sum_{k=0}^{\infty} b_k \rho^k, \tag{2.23}$$

leads to the recursion formula

$$b_{k+1} = \frac{2(k + l + 1) - \rho_0}{(k + 1)(k + 2l + 2)} b_k. \tag{2.24}$$

For large k we find

$$b_{k+1} \xrightarrow[k \to \infty]{} \frac{2}{k} b_k \tag{2.25}$$

which implies a total asymptotic behaviour

$$U_{El}(\rho) \underset{\rho \to \infty}{\propto} \exp(\rho) \tag{2.26}$$

leaving us with eigenfunctions that cannot be normalized (Shankar, 1994). Consequently, the power series (2.23) has to end at some k. This leads to the condition

$$b_{N+1} = 0 \iff 2(N + l + 1) - \rho_0 = 0. \tag{2.27}$$

Solving equation (2.27) and substituting ρ_0 with equation (2.20) yields

$$E = -\frac{\hbar^2 \kappa^2}{2\mu} = -\frac{\mu e^4}{(4\pi\epsilon_0)^2 \, 2\hbar^2 (N + l + 1)^2} \tag{2.28}$$

In terms of the Bohr radius (Bohr, 1913)

$$a_0 = \frac{4\pi\epsilon_0 \hbar^2}{me^2} \tag{2.29}$$

and the principal quantum number $n = (N + l + 1)$, the energy levels of the hydrogen atom are given by

$$E_n = -\frac{e^2}{(4\pi\epsilon_0) \, a_0} \frac{\mu}{m} \frac{1}{2n^2}. \tag{2.30}$$

In atomic units (a.u.), which will be used to the benefit of a clearer notation in the following, the physical constants of the electron mass m, the elementary charge e, the electric force constant $1/(4\pi\epsilon_0)$, and the reduced Planck constant $\hbar$ are defined so that they are unity (Bransden & Joachain, 2003). Equation (2.30) is then given by

$$E_n = -\frac{\mu}{2n^2}. \tag{2.31}$$

We see, that – in addition to the degeneracy in m – the energy eigenvalues are also independent of the quantum number l. Altogether the hydrogen atom exhibits a degeneracy of

$$\sum_{l=0}^{n-1} (2l + 1) = n^2 \tag{2.32}$$

8

for each shell n. This additional degeneracy is often called "accidental" (Shankar, 1994). However it can be explained by the conservation of a quantum mechanical analog to the Runge-Lenz vector (Pauli, 1926).

Up to the normalization the derivation of the wave functions Ψ_{Elm} follows using equation (2.21) and the recursion relation (2.24). With the power series terminating at $N = n-l-1$, the solution for $w(\rho)$ is given by the associated Laguerre polynomials $L_{n-l-1}^{2l+1}(2\rho)$, which leads to

$$\Psi_{nlm}(r, \Theta, \Phi) \propto \exp\left(-\frac{r}{na_0}\right)\left(\frac{r}{na_0}\right)^l L_{n-l-1}^{2l+1}\left(\frac{2r}{na_0}\right) Y_{lm}(\Theta, \Phi). \tag{2.33}$$

As a last point we note that the above procedure can easily be transfered to any hydrogen-like ion by substituting the proton mass with the nuclear mass in equation (2.2) and by making the shift $e^2 \to Ze^2$ in the Coulomb potential.

2.2 Energy Level Splitting

2.2.1 The Dirac Equation

Despite the foregoing description of the hydrogen atom working quite well, precise measurements show notable differences to the theoretical predictions obtained above (Bransden & Joachain, 2003). This is due to the Schrödinger equation neglecting relativistic effects. A first stepping stone to a fully relativistic equation is the relativistic energy-momentum relation

$$E = \sqrt{c^2\mathbf{p}^2 + m^2c^4}. \tag{2.34}$$

However, the way space and time are dealt with here is highly asymmetric, which can be seen by expanding the square root (Shankar, 1994). The goal is an equation containing both, time and spatial, derivatives to first order only. Such an equation was derived by Dirac (1928). Just like Dirac did, at times it is preferably to just write down what one would like to obtain. In our case, the term in the square root on the right-hand side of equation (2.34) has to be written as a perfect square

$$c^2\mathbf{p}^2 + m^2c^4 = (c\boldsymbol{\alpha} \cdot \mathbf{p} + \beta mc^2)^2 \tag{2.35}$$

whose radix is linear in $\mathbf{p}$. Equating the coefficients then yields

$$\alpha_i^2 = \beta^2 = 1 \quad (i = 1, 2, 3) \tag{2.36}$$

$$[\alpha_i, \alpha_j]_+ = \alpha_i\alpha_j + \alpha_j\alpha_i = 0 \quad (i \neq j) \tag{2.37}$$

$$[\alpha_i, \beta]_+ = 0 \tag{2.38}$$

where $[\ ,\ ]_+$ denotes the anticommutator. For these three requirements to be satisfied, α_i and β have to be 4×4 matrices (Shankar, 1994). They are unique up to unitary transformations. A common representation is given by the Pauli matrices (Pauli, 1927)

$$\boldsymbol{\alpha} = \begin{bmatrix} 0 & \boldsymbol{\sigma} \\ \boldsymbol{\sigma} & 0 \end{bmatrix}, \quad \beta = \begin{bmatrix} I & 0 \\ 0 & -I \end{bmatrix} \tag{2.39}$$

with I the 2×2 unit matrix. Knowing $\boldsymbol{\alpha}$ and β we can write down the Dirac equation

$$i\hbar\frac{d\Psi}{dt} = (c\boldsymbol{\alpha} \cdot \mathbf{p} + \beta mc^2)\Psi. \tag{2.40}$$

Note that Ψ is now a four-component vector. It is convenient to introduce the two-component spinors χ and Φ which are called the large and small components (Shankar, 1994). Separating the time dependence, equation (2.40) can now be written as

$$\begin{bmatrix} E - mc^2 & -c\boldsymbol{\sigma} \cdot \mathbf{p} \\ -c\boldsymbol{\sigma} \cdot \mathbf{p} & E + mc^2 \end{bmatrix} \begin{bmatrix} \chi \\ \Phi \end{bmatrix} = \begin{bmatrix} 0 \\ 0 \end{bmatrix}. \tag{2.41}$$

2.2.2 The Fine Structure

In order to treat the hydrogen atom by means of the Dirac equation, the Coulomb potential V has to be inserted. Equation (2.41) describes a system of two coupled differential equations. In the present case, one of these equations can be used to express Φ in terms of χ:

$$\Phi = (E + mc^2 - V)^{-1} c \boldsymbol{\sigma} \cdot \mathbf{p} \chi. \tag{2.42}$$

This leaves us with

$$(E - mc^2 - V)\chi = c \boldsymbol{\sigma} \cdot \mathbf{p} \left(\frac{1}{E + mc^2 - V} \right) c \boldsymbol{\sigma} \cdot \mathbf{p} \chi. \tag{2.43}$$

By introducing $E_{\mathrm{S}} = E - mc^2$, the denominator on the right-hand side can be expanded in $(v/c)^2$. In zeroth order equation (2.43) just reduces to the Schrödinger equation (Shankar, 1994). Thus we extend our expansion to one more order and an additional term emerges:

$$\frac{1}{E + mc^2 - V} = \frac{1}{2mc^2} \left(1 + \frac{E_{\mathrm{S}} - V}{2mc^2} \right)^{-1} \approx \frac{1}{2mc^2} - \frac{E_{\mathrm{S}} - V}{4m^2c^4}. \tag{2.44}$$

Equation (2.43) then reads

$$E_{\mathrm{S}} \chi = \left[\frac{p^2}{2m} + V - \frac{\boldsymbol{\sigma} \cdot \mathbf{p}(E_{\mathrm{S}} - V)\boldsymbol{\sigma} \cdot \mathbf{p}}{4m^2c^2} \right] \chi. \tag{2.45}$$

An unpleasant feature herein is E_{S} being found on both sides. We would like to express $(E_{\mathrm{S}} - V)$ in terms of $\mathbf{p}$. Since the concerned term should be of order $(v/c)^4$ and with the factors $\boldsymbol{\sigma} \cdot \mathbf{p}$ already delivering an order of $(v/c)^2$, we can use the Schrödinger equation to make the substitution $E_{\mathrm{S}} - V \to p^2/2m$ (Shankar, 1994). However, to do so $E_{\mathrm{S}} - V$ must act directly on χ. This can be easily achieved by evoking the commutator, a trick commonly used in quantum mechanics:

$$\begin{aligned} (E_{\mathrm{S}} - V)\boldsymbol{\sigma} \cdot \mathbf{p}\chi &= \boldsymbol{\sigma} \cdot \mathbf{p}(E_{\mathrm{S}} - V)\chi + \boldsymbol{\sigma} \cdot [E_{\mathrm{S}} - V, \mathbf{p}]\chi \\ &= \boldsymbol{\sigma} \cdot \mathbf{p}\frac{p^2}{2m}\chi + \boldsymbol{\sigma} \cdot [\mathbf{p}, V]\chi. \end{aligned} \tag{2.46}$$

With this and the fact that the Pauli matrices are the generators of a Clifford algebra (Poole & Farach, 1982) equation (2.45) becomes

$$E_{\mathrm{S}} \chi = \left[\frac{p^2}{2m} + V - \frac{p^4}{8m^3c^2} - \frac{i\boldsymbol{\sigma} \cdot \mathbf{p} \times [\mathbf{p}, V]}{4m^2c^2} - \frac{\mathbf{p} \cdot [\mathbf{p}, V]}{4m^2c^2} \right] \chi. \tag{2.47}$$

It is now a lengthy and rather technical procedure to identify the last three terms of equation (2.47) with the fine structure corrections in their typical notation

$$H_{\mathrm{rm}} = -\frac{p^4}{8m^3c^2} \tag{2.48}$$

$$H_{\mathrm{so}} = \frac{e^2}{2m^2c^2r^3} \mathbf{S} \cdot \mathbf{L} \tag{2.49}$$

$$H_{\mathrm{D}} = \frac{e^2 \hbar^2 \pi}{2m^2c^2} \delta^3(\mathbf{r}) \tag{2.50}$$

since especially in case of the Darwin term H_{D} the small component Φ has to be regarded in order to obtain a properly normalized wave function. This leads to an additional term in equation (2.47). Referring to Shankar (1994) these steps are omitted here. Let us instead turn our attention to the roots of the three extra terms and their impact on the energy eigenvalues.

The term H_{rm} solely displays the correction to the kinetic energy due to the relativistic mass increase. Since $\mathbf{p}$ does not act on spin or angular momenta, the energy adjustment through H_{rm} exclusively depends on the principal quantum number n (Bransden & Joachain, 2003).

The spin-orbit term H_{so} describes the electromagnetic interaction between the electron's spin magnetic moment and the magnetic field created in the electron's rest frame by the "proton's movement". It is

preferably treated in a different set of eigenfunctions than the $\Psi_{nlm_lm_s}$ which lead to the simultaneous diagonalization of H, L^2, L_z and S_z. The functions $\Psi_{nlm_lm_s}$ result from the earlier used eigenfunctions Ψ_{nlm} by adding the quantum number m_s. After introducing the total angular momentum

$$\mathbf{J} = \mathbf{L} + \mathbf{S} \text{ with eigenvalues } j = \begin{cases} l \pm 1/2 \ (l \neq 0) \\ 1/2 \ (l = 0) \end{cases} \tag{2.51}$$

it is evident that an eigenbasis of H, L^2, J^2 and J_z also diagonalizes $\mathbf{L} \cdot \mathbf{S}$ as

$$J^2 = L^2 + 2\mathbf{L} \cdot \mathbf{S} + S^2. \tag{2.52}$$

This leads to an energy shift of

$$\Delta E_{\text{so}} \propto j(j+1) - l(l+1) - \frac{3}{4} \tag{2.53}$$

and partly removes the degeneracy in l (Bransden & Joachain, 2003). Note that there is no contribution of the spin-orbit term to all states with $l = 0$.

The Darwin term H_{D} bears witness to the fact that the localization of a relativistic particle is restricted to its Compton wavelength. Therefore, its potential energy is not just given by $V(\mathbf{r})$, but also depends on the electric field at the surroundings of $\mathbf{r}$. Since $\Psi(\mathbf{r} = 0) \neq 0$ is only valid for electrons with $l = 0$, the energy of the remaining ones is not affected by H_{D}.

2.2.3 Additional Splitting Effects

The story of energy level splitting does not cease at this point. In 1947 W.E. Lamb and R.C. Retherford revealed an energy difference between the $2s_{1/2}$ and $2p_{1/2}$ levels[2] of hydrogen (Lamb & Retherford, 1947). An exact derivation of this "Lamb shift" can be accomplished in quantum electrodynamics (QED). Qualitatively it can be understood through the emission and absorption of virtual photons whose repulsion is leading to a jitter motion of the electron.

Just like the electron, neutrons and protons are spin-1/2 particles. If the nuclear spin, i.e., the total spin of all the neutrons and protons in the core of an atom, is taken into account, the hyperfine structure emerges. Here, the energy corrections are the results of interactions between the nuclear spin, the electron spin, and the electron's orbital angular momentum similar to the one of $\mathbf{L}$ and $\mathbf{S}$ in the fine structure.

Lastly also the degeneracy in the quantum number m can be removed. Remember that it arises because of the spherical symmetry of our problem. However, by applying an external electric or magnetic field to the atom, this symmetry is broken. The energy corrections result from the interaction of the electron's electric dipole moment or its magnetic moment with the associated external field. The corresponding phenomena are named the Stark effect (Stark, 1913) and the Zeeman effect (Zeeman, 1897) after their respective discoverers.

As elucidated by Hell (2012), none of these additional corrections is of importance at the energy regime analyzed in this thesis.

2.3 Many-electron Atoms

For atoms with two or more electrons no exact solution of the Schrödinger equation exists and one has to evoke approximations. One approach to get good estimates is given by the Ritz method (Ritz, 1909) where the parameters of a reasoned trial function are determined by means of variational calculus. With the number of electrons increasing, these calculations can get as unhandsome as you wish. The pivotal idea outlined hereafter is the central field approximation which assumes that every single electron experiences a potential V caused by the atomic nucleus as well as by the other electrons.

---

[2]The level notation here is of the form nl_j where the letters s, p, d, f, ... correspond to orbital angular momentum quantum numbers $l = 0, 1, 2, 3, \dots$

2.3.1 The Central Field Approximation

The following treatment involves an atom or ion with N electrons and a nuclear charge Ze. At first all the corrections introduced in 2.2 are disregarded and only the Coulomb potential of the nucleus and the Coulomb repulsion between electrons is taken into account. The Hamiltonian is then given by

$$H = \sum_{i=1}^{N} \left(-\frac{1}{2} \nabla_{r_i}^2 - \frac{Z}{r_i} \right) + \sum_{i<j=1}^{N} \frac{1}{r_{ij}} \tag{2.54}$$

where $\mathbf{r}_i$ denotes the coordinates of electron i and $r_{ij} = |\mathbf{r}_i - \mathbf{r}_j|$ (Bransden & Joachain, 2003). The $1/r_{ij}$ terms are what prevents any further attempts to an exact solution. We would like to treat these terms by means of perturbation theory. However, for a large number of electrons their sum will not be as negligible as necessary (Bransden & Joachain, 2003). Therefore, we split up the Hamiltonian just to add and subtract the sum $\sum_i V(r_i)$ of spherical potentials:

$$H = H_{\rm c} + H_1 \tag{2.55}$$

$$H_{\rm c} = \sum_{i=1}^{N} \left(-\frac{1}{2} \nabla_{r_i}^2 + V(r_i) \right) \tag{2.56}$$

$$H_1 = \sum_{i<j=1}^{N} \frac{1}{r_{ij}} - \sum_{i=1}^{N} \left(\frac{Z}{r_i} + V(r_i) \right). \tag{2.57}$$

The difficulty here is to choose the effective potentials $V(r_i)$ in a way that on the one hand the perturbation H_1 is sufficiently small and on the other hand the Schrödinger equation for the unperturbed Hamiltonian $H_{\rm c}$ is acceptably simple to solve. An elaborate way to determine the effective potential is via the Hartree-Fock method which will be discussed in 2.3.2 later on. But first, we want to establish two vital limits for the effective potential. For a small distance r_i of the electron i to the nucleus compared to the other electrons we have $r_{ij} \approx r_j$ and $r_i \ll r_j$. Thus the electron only "feels" the action of the nuclear Coulomb potential. In contrast, large values of r_i yield $r_{ij} \approx r_i$ and the electron sees the nucleus screened by all the other electrons. Summarizing we learn that

$$V(r) \xrightarrow[r\to 0]{} -\frac{Z}{r} \tag{2.58}$$

$$V(r) \xrightarrow[r\to\infty]{} -\frac{Z-N+1}{r}. \tag{2.59}$$

2.3.2 The Hartree-Fock Method

Via some fundamental requirements, the Hartree-Fock method builds up on the central field approach and delivers equations for every individual electron wave function. To deal with the Pauli exclusion principle (Pauli, 1925), the N-electron wave function is given by a Slater determinant

$$\Phi(q_1, q_2, \ldots, q_N) = \frac{1}{\sqrt{N!}} \sum_P (-1)^{\operatorname{sgn} P} P \underbrace{u_\alpha(q_1) u_\beta(q_2) \cdots u_\nu(q_N)}_{=:\Phi_{\rm H}} \tag{2.60}$$

which is written in terms of a sum over all permutations P of the electron coordinates q_i for the benefit of a simple notation. Note that the q_i embrace both the spatial coordinates and the spin variable of the respective electron while the letters $\alpha, \beta, \ldots, \nu$ denote a particular set of quantum numbers. We then ask for all the spin-orbitals u_λ to be orthonormal, i.e.,

$$(u_\mu, u_\lambda) := \int dq\, u_\mu^*(q) u_\lambda(q) = \delta_{\lambda\mu}. \tag{2.61}$$

We start with equation (2.54) and partition the Hamiltonian into the sum H_1 of all the single electron

Hamiltonians and the interaction term H_2, namely

$$H_1 = \sum_{i=1}^{N} \left(-\frac{1}{2}\nabla_{r_i}^2 - \frac{Z}{r_i} \right) =: \sum_{i=1}^{N} h_i \tag{2.62}$$

$$H_2 = \sum_{i<j=1}^{N} \frac{1}{r_{ij}} \tag{2.63}$$

The Hartree-Fock approach is a special form of the variational method where the correct wave functions are determined by exploiting the fact that they are stationary points of the functional

$$E[\Phi] = (\Phi, H\Phi) \tag{2.64}$$

which just represents the expectation value of the Hamiltonian in the state Φ (Shankar, 1994). Before carrying out the actual variation, let us first simplify equation (2.64). As long as the occupied states stay the same, the Hamiltonian does not notice any permutation of electron coordinates and as a consequence commutes with any permutation P. This allows us to write the expectation value of H_1 as

$$\begin{aligned}
(\Phi, H_1\Phi) &= \sum_{i=1}^{N}\sum_{P}(-1)^{\mathrm{sgn}\,P}(\Phi_{\mathrm{H}}, h_i P\Phi_{\mathrm{H}}) \\
&= \sum_{i=1}^{N}(\Phi_{\mathrm{H}}, h_i \Phi_{\mathrm{H}}) \\
&= \sum_{\lambda}\underbrace{(u_\lambda(q_i), h_i u_\lambda(q_i))}_{=:I_\lambda} \quad \lambda = \alpha, \beta, \ldots, \nu
\end{aligned} \tag{2.65}$$

where equation (2.61) was used to get from the first line to the second. The calculation for H_2 can be performed analogously:

$$\begin{aligned}
(\Phi, H_2\Phi) &= \sum_{i<j}\sum_{P}(-1)^{\mathrm{sgn}\,P}(\Phi_{\mathrm{H}}, \frac{1}{r_{ij}}P\Phi_{\mathrm{H}}) \\
&= \frac{1}{2}\sum_{\lambda}\sum_{\mu}\Bigg[\underbrace{\left(u_\lambda(q_i)u_\mu(q_j), \frac{1}{r_{ij}}u_\lambda(q_i)u_\mu(q_j) \right)}_{=:J_{\lambda\mu}} \\
&\quad - \underbrace{\left(u_\lambda(q_i)u_\mu(q_j), \frac{1}{r_{ij}}u_\mu(q_i)u_\lambda(q_j) \right)}_{=:K_{\lambda\mu}} \Bigg]
\end{aligned} \tag{2.66}$$

With these it is possible to express equation (2.64) in a simpler form, namely

$$E[\Phi] = \sum_{\lambda} I_\lambda + \frac{1}{2}\sum_{\lambda}\sum_{\mu}[J_{\lambda\mu} - K_{\lambda\mu}]. \tag{2.67}$$

Starting from here, we are now ready to look at the variations of the spin-orbitals u_λ in order to find the actual wave functions. Note, however, that due to the requirement of orthonormality the method of Lagrange multipliers calls for the functional

$$\begin{aligned}
\mathcal{L}[\Phi] &= E[\Phi] + \sum_{\lambda}\sum_{\mu}\epsilon_{\lambda\mu}(\delta_{\lambda\mu} - (u_\lambda, u_\mu)) \\
&= E[\Phi] + \sum_{\lambda}E_\lambda(1 - (u_\lambda, u_\lambda))
\end{aligned} \tag{2.68}$$

to be "minimized" rather than the actual functional $E[\Phi]$ alone (Bransden & Joachain, 2003). In the second line of equation (2.68), the matrix $\epsilon_{\lambda\mu}$ of Lagrange multipliers was assumed to be diagonal

without loss of generality as this can always be achieved through an appropriate unitary transformation. The variation of the u_λ^* then yields

$$
\begin{aligned}
\delta\mathcal{L} = \delta\Bigg(&\sum_\lambda (u_\lambda(q_i), h_i u_\lambda(q_i)) + \frac{1}{2} \sum_{\lambda,\mu} \Bigg[\left(u_\lambda(q_i) u_\mu(q_j), \frac{1}{r_{ij}} u_\lambda(q_i) u_\mu(q_j) \right) \\
&- \left(u_\lambda(q_i) u_\mu(q_j), \frac{1}{r_{ij}} u_\mu(q_i) u_\lambda(q_j) \right) \Bigg] + \sum_\lambda E_\lambda (1 - (u_\lambda(q_i), u_\lambda(q_i))) \Bigg) \\
= &\, h_i u_\gamma(q_i) + \sum_\mu \underbrace{\left(u_\mu(q_j), \frac{1}{r_{ij}} u_\mu(q_j) \right)}_{=: V_\mu^{\mathrm{d}}(q_i)} u_\gamma(q_i) \\
&- \sum_\mu \underbrace{\left(u_\mu(q_j), \frac{1}{r_{ij}} u_\gamma(q_j) \right) u_\mu(q_i)}_{=: V_\mu^{\mathrm{ex}}(q_i) u_\gamma(q_i)} - E_\gamma u_\gamma(q_i) \overset{!}{=} 0 \quad \forall \gamma
\end{aligned}
\tag{2.69}
$$

where we have defined the direct operator V_μ^{d} and the exchange operator V_μ^{ex}. The term containing the direct operators can be interpreted as the mean Coulomb potential of all the other electrons on the i-th one. The exchange operator has no classical analogon. It only acts on electrons with the same spin variable and by doing so manifests the Pauli exclusion principle due to lowering the total interaction energy by keeping these electrons apart (Bransden & Joachain, 2003). The equations (2.69) are called the Hartree-Fock equations. By applying the introduced operators, these equations are

$$
\Bigg[-\frac{1}{2} \nabla_{r_i}^2 \underbrace{- \frac{Z}{r_i} + \sum_\mu V_\mu^{\mathrm{d}}(q_i) - \sum_\mu V_\mu^{\mathrm{ex}}(q_i)}_{= \mathcal{V}(q_i)} \Bigg] u_\gamma(q_i) = E_\gamma u_\gamma(q_i).
\tag{2.70}
$$

While they do look like single particle Schrödinger equations, we note that $\mathcal{V}$ delicately depends on all spin-orbitals u_μ via the direct and exchange operators. As a result the Hartree-Fock equations can only be solved iteratively (Bransden & Joachain, 2003). The general procedure thereby is outlined in the following:

1. Start with a particular set of spin-orbitals $u_\alpha^1, u_\beta^1, \ldots, u_\nu^1$

2. Calculate $\mathcal{V}$

3. Solve equation (2.70) for $\mathcal{V} \to u_\alpha^2, u_\beta^2, \ldots, u_\nu^2$

4. Goto 2.

The iteration proceeds until the difference of $\mathcal{V}^n$ and $\mathcal{V}^{n-1}$ is sufficiently small. The Hartree-Fock method is therefore called a self-consistent field method.

The Slater determinant composed of the final spin-orbitals $u_\alpha^n, u_\beta^n, \ldots, u_\nu^n$ is known as the Hartree-Fock wave function Ψ_{HF}. The associated energy expectation value is given by

$$
E_{\mathrm{HF}} = (\Psi_{\mathrm{HF}}, H\Psi_{\mathrm{HF}}).
\tag{2.71}
$$

2.3.3 Corrections and Coupling Schemes

The determination of the Hartree-Fock energy E_{HF} is of course not the whole story. Through the Hartree-Fock potential $\mathcal{V}(q_i)$ the terms in equation (2.55) are well-defined. Possibly $\mathcal{V}(q_i)$ has to be averaged over the angles and the spin coordinate to provide a central potential $\mathcal{V}(r_i)$ since the Hartree-Fock potential is not spherically symmetric as soon as one subshell is incomplete (Bransden & Joachain, 2003). H_1 then contains all the corrections between the Hartree-Fock potential and the actual exact non-relativistic Coulomb interactions. These varieties could now be treated by means of perturbation theory (Bransden & Joachain, 2003). We note, however, that further adjustments have to be made.

Table 2.1: The possible terms for the electron configurations $np\,n'p$ and np^2.

electron configuration	possible terms
$np\,n'p$	$^1\mathrm{S},^1\mathrm{P},^1\mathrm{D},^3\mathrm{S},^3\mathrm{P},^3\mathrm{D}$
np^2	$^1\mathrm{S},^1\mathrm{D},^3\mathrm{P}$

Fundamentally, just like for the hydrogen atom relativistic effects have to be taken into account. For a many-electron atom, the spin-orbit term is by far the most dominant of the effects discussed in 2.2.2 (Bransden & Joachain, 2003). That leads to an additional term in the total Hamiltonian:

$$H = H_{\mathrm{c}} + H_1 + H_2 \tag{2.72}$$

$$H_2 = \sum_i \zeta(r_i)\mathbf{L}_i \cdot \mathbf{S}_i \tag{2.73}$$

$$\zeta(r_i) = \frac{1}{2m^2\mathrm{c}^2 r_i}\frac{\mathrm{d}V}{\mathrm{d}r_i}(r_i). \tag{2.74}$$

Now both H_1 and H_2 are perturbing terms and the manner of performing the perturbation is subject to their relative strength. Here only the cases $H_1 \gg H_2$ and $H_2 \gg H_1$ are considered. The first one leads to the so called L-S (or Russell-Saunders) coupling while the second one is referred to as jj coupling. The intermediate coupling case where $H_1 \approx H_2$ is highly delicate and will not be tackled in this thesis.

L-S coupling

With H_1 being the dominant perturbing term, H_2 is ignored in the first step. Hence we deal with the Hamiltonian $H = H_{\mathrm{c}} + H_1$ again. The total orbital angular momentum $\mathbf{L}$ as well as the total spin angular momentum $\mathbf{S}$ commute with H which can easily be verified owing to the lack of spin-orbit coupling. This gives rise to the application of the term symbols ^{2S+1}L to describe the energy eigenvalues.

For a particular electron configuration the possible terms can be obtained via the rules for the addition of angular momenta. Briefly worded, they state that the allowed values for the total orbital angular momentum quantum number L resulting from the addition of $\mathbf{L}_1$ and $\mathbf{L}_2$ with quantum numbers l_1 and l_2 are

$$L = |l_1 - l_2|, |l_1 - l_2| + 1, \ldots, l_1 + l_2. \tag{2.75}$$

Exactly the same relation holds for the addition of spin angular momenta. Note that the only accessible term for a closed subshell is $^1\mathrm{S}$ (Bransden & Joachain, 2003). Due to the Pauli exclusion principle special attention is required if the added angular momenta belong to electrons of the same subshell. Concerning this, look at Table 2.1 for a brief example.

In the second step, we reconsider H_2. Now the Hamiltonian does not commute with $\mathbf{L}$ and $\mathbf{S}$, but with the total angular momentum $\mathbf{J}$. Every term ^{2S+1}L therefore splits into $2S + 1$ ($L \geq S$) or $2L + 1$ ($L < S$) fine structure components denoted by the Russell-Saunders symbols $^{2S+1}L_J$ and the degeneracy is removed in parts. An example is shown in Fig. 2.1.

jj coupling

The regime of jj coupling – where H_2 is of more importance relative to H_1 – is entered for high atomic numbers Z (Bransden & Joachain, 2003). In particular it is employed in order to study highly charged ions since in that case the impact of H_1 is cut down based on the lower number of electrons. In the first step of the perturbation only the spin-orbit interaction is added to the central Hamiltonian H_{c}. The resulting Hamiltonian can be written as a sum of individual Hamiltonians, namely

$$H = H_{\mathrm{c}} + H_2 = \sum_i -\frac{1}{2}\nabla_{r_i}^2 + \mathcal{V}(r_i) + \zeta(r_i)\mathbf{L}_i \cdot \mathbf{S}_i. \tag{2.76}$$
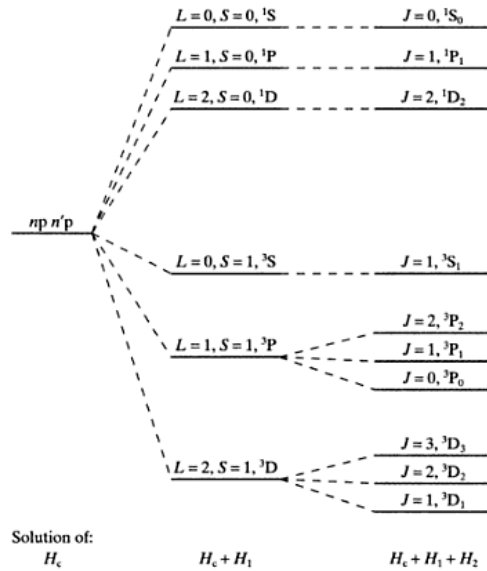
Figure 2.1: Splitting of the electron configuration $np\,n'p$ in L-S coupling (Bransden & Joachain, 2003).
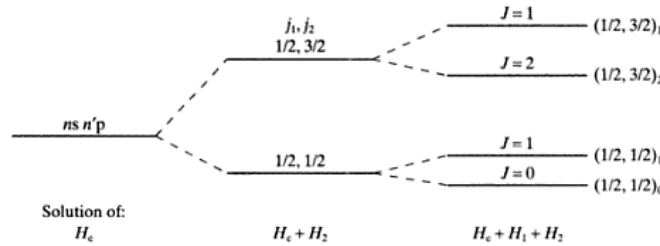

Figure 2.2: Splitting of the electron configuration $ns\,n'p$ in j-j coupling (Bransden & Joachain, 2003).

Entirely analogously to the treatment of the spin-orbit term in the fine structure of the hydrogen atom in section 2.2.2, we diagonalize $\mathbf{L}_i \cdot \mathbf{S}_i$ for all i by evoking $\mathbf{J}_i = \mathbf{L}_i + \mathbf{S}_i$. Then every eigenvalue of H is characterized by the corresponding quantum numbers $j_1, j_2, \ldots, j_N$.

The perturbation of H_1 in a second step then leads to further splitting with respect to the total angular momentum quantum number J. Hence a elaborate notation for the spectral terms has to include all the j_i and J. Usually, the former are written in parentheses while the latter is denoted as a subscript. A general term symbol thus is represented by $(j_1, j_2, \ldots, j_N)_J$. An example is depicted in Fig. 2.2.

In order to display the entire information about one term, the subshell of each electron must also be denoted. Additionally, the genesis of the coupling can be outlined by introducing intermediate quantum numbers J_i. Thus, the term symbols that we will employ later are in the form of

$$(\ldots ((nl_{j_1} nl_{j_2})_{J_1})nl_{j_3})_{J_2} \ldots)_J \tag{2.77}$$

where the intermediate quantum number J_1 specifies the coupling of j_1 and j_2. If there is only one possible value for any J_i, e.g., for a closed subshell, the notation of that number will be omitted.

2.4 Atoms and Electromagnetic Radiation

Having dealt with the energy levels in atoms, we now turn our focus on the origin of spectral lines. Therefore we shall discuss the interaction of an atom with radiation. There are three fundamental mechanisms to look at. First of all an electron's transition from a higher to a lower energy state in the atom can be realised spontaneously through emission of a photon. In addition, the same transition can be enforced by photons of external radiation fields. Lastly, these photons can also be absorbed

and lead to the inverse transition. One refers to these processes as spontaneous emission, stimulated emission, and absorption (Bransden & Joachain, 2003). In what follows, we will treat the radiation field completely classically and derive formulas for the transition probabilities. In the case of spontaneous emissions we will follow the argumentation of Einstein (1917).

2.4.1 Atoms in Electromagnetic Fields

Maxwell's equations allow the treatment of electric and magnetic fields via a scalar potential ϕ and a vector potential $\mathbf{A}$. In Coulomb gauge, i.e., $\nabla \mathbf{A} = 0$, and radiation gauge, i.e., $\phi \equiv 0$, an N-electron atom's Hamiltonian is given by (Bransden & Joachain, 2003)

$$
\begin{aligned}
H(t) &= \frac{1}{2m} \sum_{i=1}^{N} [-i\hbar \nabla_{r_i} + e\mathbf{A}(\mathbf{r}_i, t)]^2 + V \\
&= \underbrace{-\frac{\hbar^2}{2m} \sum_{i=1}^{N} \nabla_{r_i}^2 + V}_{=:H_0} \underbrace{-i\hbar \frac{e}{m} \sum_{i=1}^{N} \mathbf{A}(\mathbf{r}_i, t) \cdot \nabla_{r_i} + \frac{e^2}{2m} \sum_{i=1}^{N} \mathbf{A}^2(\mathbf{r}_i, t)}_{=:H_{\text{int}}(t)}
\end{aligned}
\tag{2.78}
$$

where H_0 is just the ordinary Hamiltonian describing the atom in the absence of any radiation field whereas the interaction is entirely covered by H_{int}. In the following derivation, we shall exclusively regard small fields. Thus the $\mathbf{A}^2$ term is disregarded, yielding

$$
H_{\text{int}}(t) \approx H'(t) = -i\hbar \frac{e}{m} \sum_{i=1}^{N} \mathbf{A}(\mathbf{r}_i, t) \cdot \nabla_{r_i}.
\tag{2.79}
$$

The time-dependent Schrödinger equation then is

$$
i\hbar \frac{\mathrm{d}}{\mathrm{d}t} \Psi(t) = \left[H_0 + H'(t) \right] \Psi(t)
\tag{2.80}
$$

where $H'(t)$ will be handled as a perturbation. The dependence on the electron coordinates $\mathbf{r}_i$ is suppressed in the current notation. Let E_k and Ψ_k then denote the eigenvalues and eigenfunctions of the unperturbed Hamiltonian, namely

$$
H_0 \Psi_k = E_k \Psi_k.
\tag{2.81}
$$

With the Ψ_k representing a complete set, any solution of the unperturbed system can be expanded as

$$
\Psi(t) = \sum_k b_k(t) \Psi_k \exp\left(-\frac{i}{\hbar} E_k t \right).
\tag{2.82}
$$

By inserting this expansion into equation (2.80) and using equation (2.81), a system of coupled differential equations for the coefficients $b_b(t)$

$$
\frac{\mathrm{d}}{\mathrm{d}t} b_b(t) = (i\hbar)^{-1} \sum_k H'_{bk}(t) b_k(t) \exp(i\omega_{bk} t)
\tag{2.83}
$$

can be obtained through the projection on the Ψ_b (Bransden & Joachain, 2003) where

$$
H'_{bk}(t) = (\Psi_b, H'(t)\Psi_k)
\tag{2.84}
$$

$$
\omega_{bk} = \frac{E_b - E_k}{\hbar}.
\tag{2.85}
$$

Assuming that the system is in the eigenstate Ψ_a before the radiation is switched on, the simultaneous equations (2.83) can be solved by integration, namely

$$
b_b(t) = (i\hbar)^{-1} \int_0^t \mathrm{d}t' \, H'_{ba}(t') \exp(i\omega_{ba} t').
\tag{2.86}
$$

If the vector potential is given in the general form

$$\mathbf{A}(\mathbf{r}, t) = \boldsymbol{\epsilon} \int_0^\infty \mathrm{d}\omega \, A_0(w) \cos(\mathbf{k} \cdot \mathbf{r} - \omega t + \alpha_\omega) \tag{2.87}$$

of an expansion in plane waves, where $\boldsymbol{\epsilon}$ indicates the polarisation and α_ω a random phase factor, $b_b(t)$ can be shown to vanish unless

$$\omega_{ba} \approx \pm\omega. \tag{2.88}$$

The connection of the states a and b through the absorption or emission of a photon with energy $\hbar\omega$ somewhat naturally follows (Bransden & Joachain, 2003).

2.4.2 Transition Rates

The squared norm of the coefficient $b_b(t)$ can be interpreted as the probability to find the system in the state b at time t (Bransden & Joachain, 2003). Calculating the time derivative of this quantity yields an expression for the likeliness of a transition from state a to state b. Depending on whether the said transition results from an absorption or an emission, the labels a and b are possibly interchanged so that the state b is always the one with higher energy. The transition rates for absorption W_{ba} and for stimulated emission $\bar{W}_{ab}$ are then introduced as

$$W_{ba} = \frac{4\pi^2}{m^2 \mathrm{c}} \left(\frac{\mathrm{e}^2}{4\pi\epsilon_0} \right) \frac{I(\omega_{ba})}{\omega_{ba}^2} \left| M_{ba}(\omega_{ba}) \right|^2 \tag{2.89}$$

$$\bar{W}_{ab} = \frac{4\pi^2}{m^2 \mathrm{c}} \left(\frac{\mathrm{e}^2}{4\pi\epsilon_0} \right) \frac{I(\omega_{ba})}{\omega_{ba}^2} \left| \bar{M}_{ab}(\omega_{ba}) \right|^2 \tag{2.90}$$

where we defined the intensity

$$I(\omega) = \frac{1}{2}\epsilon_0 \mathrm{c}\omega^2 A_0^2(\omega) \tag{2.91}$$

and the matrix elements

$$M_{ba} = N \left(\Psi_b, \exp(\mathrm{i}\mathbf{k} \cdot \mathbf{r})\boldsymbol{\epsilon} \cdot \nabla_r \Psi_a \right) \tag{2.92}$$

$$\bar{M}_{ab} = N \left(\Psi_a, \exp(-\mathrm{i}\mathbf{k} \cdot \mathbf{r})\boldsymbol{\epsilon} \cdot \nabla_r \Psi_b \right). \tag{2.93}$$

After integrating the matrix elements by parts,

$$\bar{M}_{ab} = -M_{ba}^* \tag{2.94}$$

is quickly verified (Bransden & Joachain, 2003). Since only the squared norms of these terms appear in equations (2.89) and (2.90), equation (2.94) implies

$$\bar{W}_{ab} = W_{ba} \tag{2.95}$$

in accordance with the principle of detailed balance, which states that – in equilibrium – any transition between two states is as probable as its reverse process. This principle was first formulated by Boltzmann (1872) in the context of collisions of gas particles.

2.4.3 The Einstein Coefficients and Spontaneous Emission

The classical treatment of the radiation field led to the neglect of spontaneous emissions in the calculation of $\bar{W}_{ab}$ (Bransden & Joachain, 2003). While the same treatment by means of QED would give the correct answer in a straightforward way, we will make a small detour and express the transition rate for spontaneous emission W_{ab}^{s} relative to $\bar{W}_{ab}$ following the work of Einstein (1917) and using the principle of microreversibility.

Let a and b denote two states of an atom. Considering a large number of such atoms, let N_a and N_b furthermore denote the number of atoms in the respective state. The numbers of transitions per time are then given by

$$\dot{N}_{ba} = W_{ba} N_a = B_{ba} N_a \frac{I(\omega_{ba})}{\text{c}} \tag{2.96}$$

$$\dot{N}_{ab} = \left(\bar{W}_{ab} + A_{ab}\right) N_b = \left(B_{ab} \frac{I(\omega_{ba})}{\text{c}} + A_{ab}\right) N_b \tag{2.97}$$

where we defined the Einstein coefficients B_{ba} for absorption, B_{ab} for stimulated emission, and A_{ab} for spontaneous emission. In equilibrium we expect

$$\dot{N}_{ba} = \dot{N}_{ab} \tag{2.98}$$

which yields

$$\frac{N_b}{N_a} = \frac{B_{ba}\rho(\omega_{ba})}{A_{ab} + B_{ab}\rho(\omega_{ba})} \quad \text{with } \rho(\omega) = \frac{I(\omega)}{\text{c}}. \tag{2.99}$$

On the one hand, this ratio must be equal to a Gibbs-Boltzmann distribution (Gibbs, 1902), i.e.,

$$\frac{N_b}{N_a} = \exp\left(-\frac{\hbar\omega_{ba}}{k_{\text{B}}T}\right). \tag{2.100}$$

On the other hand, the energy density $\rho(\omega)$ should follow Planck's law (Planck, 1900), i.e.,

$$\rho(\omega) = \frac{\hbar\omega^3}{\pi^2 \text{c}^3} \frac{1}{\exp\left(\hbar\omega/(k_{\text{B}}T)\right) - 1}. \tag{2.101}$$

To fulfill both of these requirements, the Einstein coefficients must obey the relations

$$B_{ba} = B_{ab} \tag{2.102}$$

$$A_{ab} = \frac{\hbar\omega_{ba}^3}{\pi^2 \text{c}^3} B_{ab}. \tag{2.103}$$

Identifying W_{ab}^{s} with A_{ab} then gives the aspired transition rate for spontaneous emission.

In an electron beam ion trap, the excitations are realised through electron-atom collisions and the radiation field does not play a major role. Thus, among all the deexcitation processes leading to the emission of a photon, spontaneous emissions are the most dominant.

Chapter 3

Measurements

3.1   EBIT/ECS

The ions which are investigated in this thesis where produced and monitored in an electron beam ion trap at the Lawrence Livermore National Laboratory (LLNL). The very first electron beam ion trap (EBIT) was installed there in 1986 to provide an alternative and, in comparison to accelerator experiments, rather small sized method for the study of highly charged ions, as its quasi precursor, the electron beam ion source (EBIS), has not been too successful at this (Levine et al., 1989). The first measurements surpassed the expectations. The containment times were longer than predicted and plasma instabilities that heat the ions could be reduced with respect to EBIS (Levine et al., 1988).

Figure 3.1 shows a sketch of an EBIT. Basically, it consists of three main parts: an electron gun to provide the actual beam, an ion trap, and a collector. Through collisions with the beam electrons, any injected gas can be ionized. The ions are then confined to the trapping region for further investigations. The whole apparatus is operating in ultra high vacuum.

The ion trap is built of three cylindrical drift tubes. The middle drift tube has a negative potential with respect to the other two, forming a potential well for positively charged ions in axial direction. In radial direction the ions are confined through the potential of the electron beam's space charge. Six radial ports in the middle tube allow for access to the trapping region. They are used for the installation of various spectrometers and to inject lowly ionized or neutral gases into the trap. The actual trap has a length of 2 cm (Levine et al., 1988) and is located in the center of an axial magnetic field provided by a pair of superconducting Helmoltz coils. Through the magnetic field, the electron beam is compressed. This process is supported by a focus electrode right after the electron gun. Since the emission rate in X-rays is proportional to the beam's current density, as pointed out by Marrs (2008), the whole point of compressing the beam is to achieve a higher count rate.

The electron gun is mainly made of a cathode coated with tungsten and barium oxide. The electron beam is generated through thermionic emission of the coating material's electrons. Through the gun anode the beam current can be adjusted (Levine et al., 1989), while the beam energy is determined by the drift tube potential minus the space charge. After traversing the trap, the beam electrons are dumped into a collector, which consists of cooled copper electrodes. In order to protect the electrodes, another magnet is operated along with them. It counteracts the field of the Helmholtz coils and consequently causes the beam to expand.

Our spectra were actually taken with SuperEBIT, a high energy variant of EBIT with a floating gun that was put into operation at LLNL in 1992. While EBIT is usually operated with beam currents around 100 mA and beam energies of about 10 keV, SuperEBIT allows for electron beam energies up to nearly 250 keV (Beiersdorfer et al., 2003).

The emission spectra were recorded with the EBIT calorimeter spectrometer (ECS), which has been operating at LLNL since 2007 (Porter et al., 2008). It was built at NASA's Goddard Space Flight Center. ECS consists of 32 pixels, each of which can thermally detect incident X-ray photons. The whole detector array is shown in Fig. 3.2. Eighteen of the 32 pixels are midband pixels taking care of an energy range from 0.1 to 10 keV, while 14 are designed to work in the high energy domain between 0.5 and 100 keV.
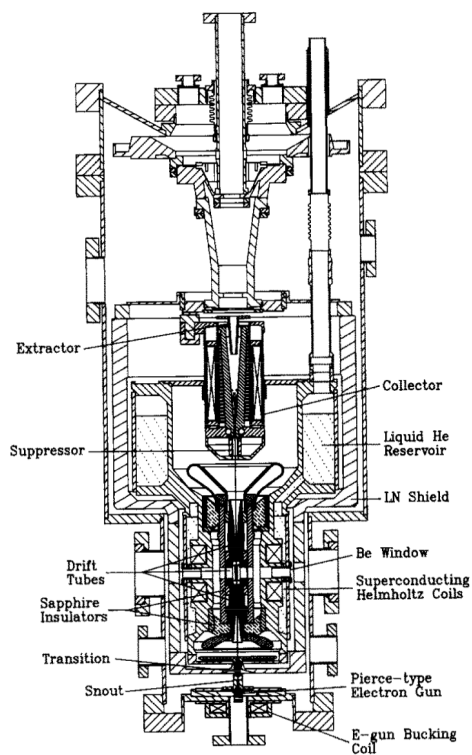
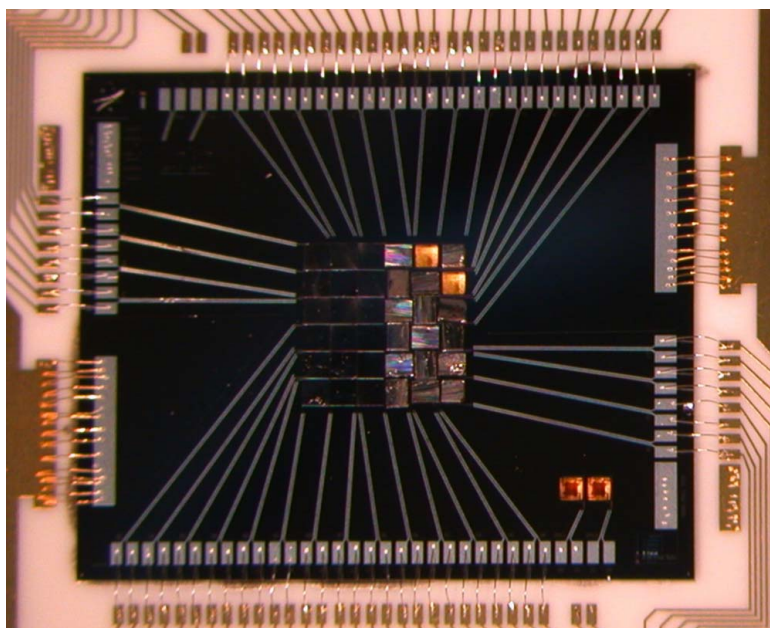Figure 3.1: Cross sectional sketch of EBIT (Levine et al., 1989).

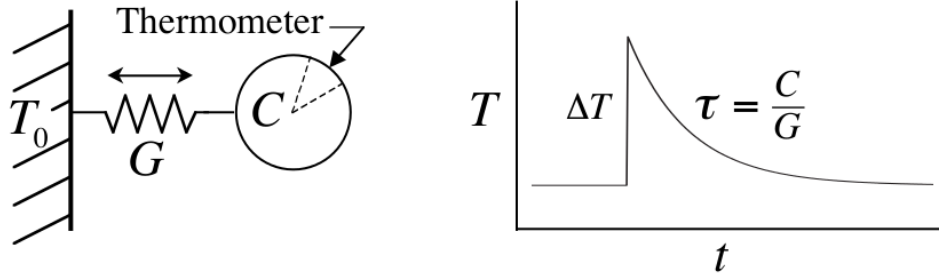Figure 3.2: The 36 pixel array of the ECS detector (Porter et al., 2008).

Figure 3.3: Sketch of a basic calorimeter. Response in the temperature domain to an incident photon (McCammon, 2005).

Each pixel can be thought of as a basic calorimeter consisting of three main parts: an absorber, a thermistor, and a heat sink (McCammon, 2005). This setup is depicted in Fig. 3.3. Every time a photon hits the absorber, its energy is thermalized there. Thus, the absorber has to be opaque in the desired energy range and provide both fast thermalization and a low heat capacity. The last point guarantees the resulting change in temperature to be rather large and therefore easier to measure. The thermistor, a resistor whose resistance sensitively depends on its temperature, is connected with the absorber through a thermal link. Because of its high values, the thermistor's resistance is determined by measuring the voltage drop across it, while being subject to a constant current. Finally, another thermal link couples the thermistor to a heat sink, which, through various cooling systems (Porter et al., 2008), brings the pixel back to a temperature of about $50\,\mathrm{mK}$. The strength of said thermal link has to be chosen wisely. The photon's total energy will not be captured if the link is too strong, while a weak link will inevitably prolong the detector's dead time. A typical temperature change after the absorption of a photon is shown in Fig. 3.3, where C denotes the absorber's heat capacity, G the conductivity of the thermal link to the heat sink, and τ the characteristic decay time.

3.2 Spectral Data

During the measurement, each photon event was recorded and given, among others, a time stamp, an index indicating the relevant pixel, and the voltage drop across the thermistor. In order to deduce the photon's energy from this data, ECS has to be calibrated. This is discussed in greater detail in section 3.3. Here only the guiding principle is mentioned. Several calibration spectra are additionally recorded. In our experiment, sulfur, silicon, neon, and argon itself were used for that purpose.

The calibration spectra must contain transition lines which cover the energy range of interest and have well established reference values. Therefore, the charge balance was caused to tend towards H- and He-like ionization states in all these measurements. The entire measured data is presented in Fig. 3.4. The single spectra are labeled with the corresponding element's symbol and, if required, with a number.

An elaborate variation of EBIT's parameters is necessary to produce the aspired charge balance. To produce the H- and He-like ionization states, the electron beam has to be extremely focused and the trap potential rather flat. The first point ensures a high collision rate, while through the second one only highly charged ions are kept in the trap, since the trap's potential, seen by the ions, strongly depends on their charge. Accordingly, the trap is deepened and the beam widened once the production of lower charge states is on the agenda. More importantly, the trap was dumped in cyclic intervals to counter the accumulation of high charge states and to get rid of unwanted heavy elements that build up in the trap over time. Primarily, the last point concerns tungsten and barium atoms emitted from the electron gun. Since the atomic mass of both these elements is larger in comparison with the injected gases, momentum conservation would cause the lighter elements to be kicked out of the trap. However, the performance of the experimental setup does inevitably change slightly from day to day. For instance, leftover foreign atoms of a previous measurement might influence the charge balance in
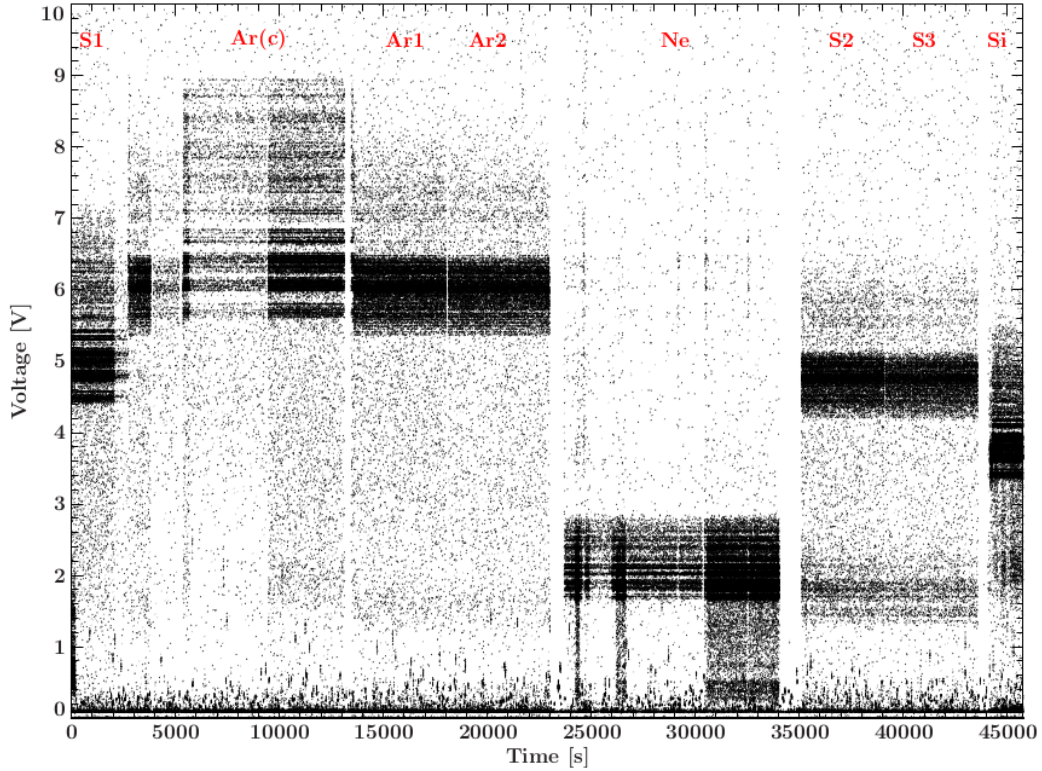
Figure 3.4: The measured data. The argon spectra of interest are denoted by Ar1 and Ar2, the argon calibration spectra by Ar(c).

the trap. Thus, the final set of parameters is usually found by trial and error.

3.3 Calibration

3.3.1 Drifts

As mentioned in the previous section, the changes in the daily performance of our experimental setup require thorough fine tuning. In particular, this applies to ECS. Since the idea behind the whole measuring apparatus is to be very sensitive to temperature changes, the cooling of the pixels needs to be spot-on. Small temperature fluctuation in the pixels might lead to drifts of the line positions in the voltage space, i.e., the function describing the relation between voltage and energy space might be slightly time-dependent. Among others, the various calibration spectra of S were recorded to check the order of these drifts. Therefore, they were run at the beginning and towards the end of the entire measurement (see Fig. 3.4). Additionally, they would allow for adjustments by interpolating between the single calibration spectra, should the drifts be too severe, and thus make for a high resolution nevertheless.

The inspection of the drifts was carried out by reading in the data of the calibration spectra labeled by S1 and S2 in Fig. 3.4 individually for every of the 16 used pixels and fitting a Gaussian function to a specific calibration line. The Interactive Spectral Interpretation System (ISIS; Houck & Denicola, 2000) was used for this purpose. See Fig. 3.5 for an example. The differences between the fitted line centers are listed in Table 3.1 along with their respective errors. By using the final results of the later calibration (see section 3.3.2), the drifts can also be evaluated in terms of the detected energy. Here, the mean of the drift amplitudes was determined to $0.25\,\mathrm{eV}$. More importantly, the determined drift values lie inside the error bars for all but two pixels and are consistent with a drift of $0\,\mathrm{eV}$ within the error bars. Thus, the observed drifts are assumed to result from statistical fluctuations and not to follow any major trend. In a first attempt to get a good calibration, all the available calibration data, i.e., one calibration spectrum of every element, was used. More precisely, the spectra labeled by S1, Ar(c), Ne, and Si in Fig. 3.4 were picked.

23

Table 3.1: Shift of the line centers for every pixel.

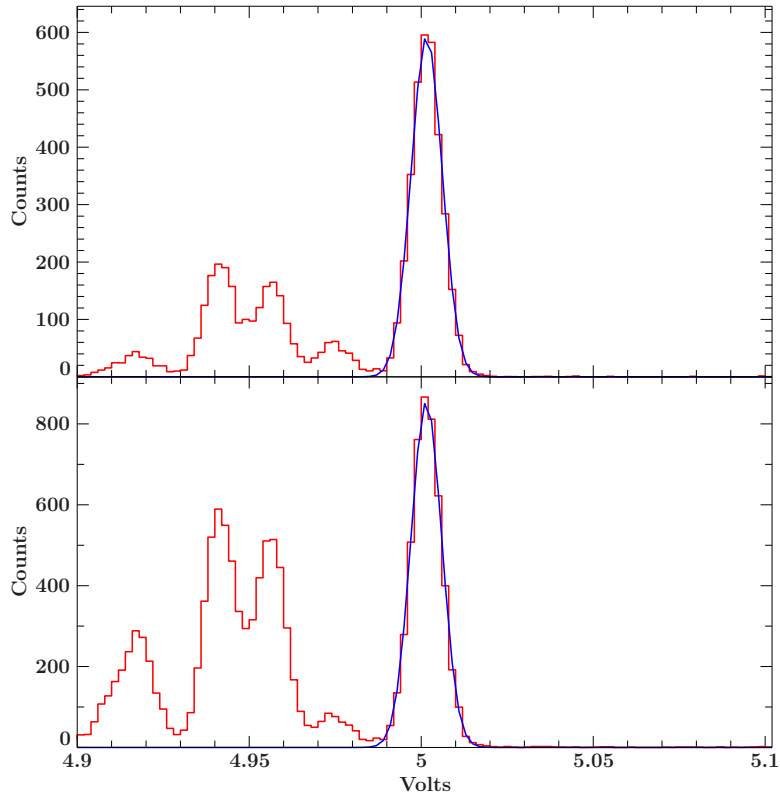| Pixel	Drift [mV]
0	0.3 ± 0.9
1	-0.2 ± 1.0
2	1 ± 8
3	0.9 ± 0.8
4	1.4 ± 0.8
6	0.6 ± 1.0
7	-0.2 ± 0.9
15	0.4 ± 0.9
24	-0.3 ± 0.9
25	0.3 ± 0.9
26	-0.1 ± 1.0
27	0.7 ± 1.0
28	-0.0 ± 1.0
29	-0.0 ± 0.9
30	-0.5 ± 1.0
31	0.5 ± 1.1

Figure 3.5: A Gaussian function fitted to the calibration spectra S1 (top) and S2 (bottom).

3.3.2 The CXRS Package

Since all the pixels slightly differ in their geometry and quality structure, they have to be calibrated separately. To automatize this task, Ming Feng Gu wrote the so called CXRS package, which is ordinarily used to calibrate ECS. It builds upon the assumption that the spectral key features are the same in each pixel. To start off the calibration, the events of each pixel are binned to a histogram with a bin size of $0.002\,\mathrm{V}$. These histograms are then shifted, stretched, and compressed to match a reference pixel. A file containing the scaling functions is created. It is invoked at a later time to assign the calibration lines to their corresponding voltage in every pixel. At this point, the single pixel spectra are checked for any suspicious distinctions between themselves. All such must be considered at the selection of the calibration lines (see below). Next, the histograms are added in the reference pixel scale. In the added spectrum, the calibration lines are selected by hand. Their energies have to be well known. Therefore, the choice falls on the H-like Lyman- and the He-like K-series. These systems are sufficiently simple and accurate, experimentally validated calculations of their transition energies exist (see, e.g., Gabriel, 1972; Drake, 1988; Vainshtein & Safronova, 1985; Garcia & Mack, 1965; Johnson & Soff, 1985). A Gaussian line is fitted to each calibration line. By using the scaling functions the respective line centers are determined for all pixels. A polynomial function of fourth order is then fitted to the resulting pairs of voltage and energy, yielding the aspired connection between the two quantities. In an ideal pixel, no voltage drop is logged as long as there is no incident photon. Hence, the constant factor in the polynomial is set at zero and at least four calibration lines are necessary to determine it decidedly.

From Ne and Ar, the lines $K\alpha$ to $K\delta$ and $Ly\,\alpha$ to $Ly\,\gamma$ were used. In the spectra of S and Si, $Ly\,\beta$ blends with $K\delta$ and $K\epsilon$ respectively. These lines were therefore omitted. Thus, from the Lyman series only $Ly\,\alpha$ was made use of in both cases, while $K\alpha$ to $K\gamma$ were taken into account for S and $K\alpha$ to $K\delta$ for Si. That way, an energy range from about $1\,\mathrm{keV}$ all the way up to above $4\,\mathrm{keV}$ was well sampled with calibration lines. The reference values for the Lyman series were taken from Garcia & Mack (1965). As far as the $K\alpha$-lines are concerned, the values come from Drake (1988). The energies of higher transitions in the K-series, i.e., up to $K\delta$, can be found in Vainshtein & Safronova (1985). However, as shown by Beiersdorfer et al. (1989), their values display obvious discrepancies to experimental data. Having said that, the deviations are nearly the same for all transitions. Hence, the gaps between them actually fit the experimental results quite well. Consequently, $K\beta$ to $K\delta$ originate from Vainshtein & Safronova (1985), but were adjusted to match the ground states of Drake (1988). Most of the used reference values are given in units of kayser $= \mathrm{cm}^{-1}$. The employed conversion factor[3] is $1\,\mathrm{cm}^{-1} = 1.239841930 \cdot 10^{-4}\,\mathrm{eV}$.

With regard to the evaluation of the low charge argon spectra, the quality of the calibration is the be-all and end-all. The goodness of the calibration can be quantified by applying the stated polynomials to the fitted line centers and comparing the results with the reference values. Since more than four calibration lines have been used, no exact congruence is expected. This is based on the fact that the polynomial of fourth order is a too elementary function to describe the precise correlation between measured voltage drop and photon energy. Over- and underestimations of the reference values for different pixel would then lead to artificial broadening of the spectral components and therefore downgrade the resolution. If the differences should tend to be either positive or negative for all the pixels, the resolution will not be affected as drastically, but the energy of the line centers will be off. Because of the large number of calibration lines, differences of several eV emerged. By constraining the calibration lines to the actual range of interest around 2900 and $3200\,\mathrm{eV}$, the quality of the calibration could notably be improved. The calibration lines of Ne and Si were completely neglected. Some of the higher transitions in Ar and S were also ignored, assuming that their fits have not been the best due to their lower count rates. Ultimately, only Ar $Ly\,\alpha$, $Ly\,\beta$, $K\alpha$, and $K\beta$ as well as S $Ly\,\alpha$, $K\alpha$, $K\beta$, and $K\gamma$ were left over. Hereby, the mean absolute value of the differences between the fitted line centers and their reference values could be reduced from 0.63 to $0.09\,\mathrm{eV}$. For one pixel, the quality of the calibration is illustrated in Fig. 3.6.

After this final calibration, the detected events can be transfered into energy space. A histogram with a

---

[3]It is taken from the NIST Reference on Constants, Units, and Uncertainty `http://physics.nist.gov/cgi-bin/cuu/Convert?exp=0&num=1&From=minv&To=ev&Action=Only+show+factor`.
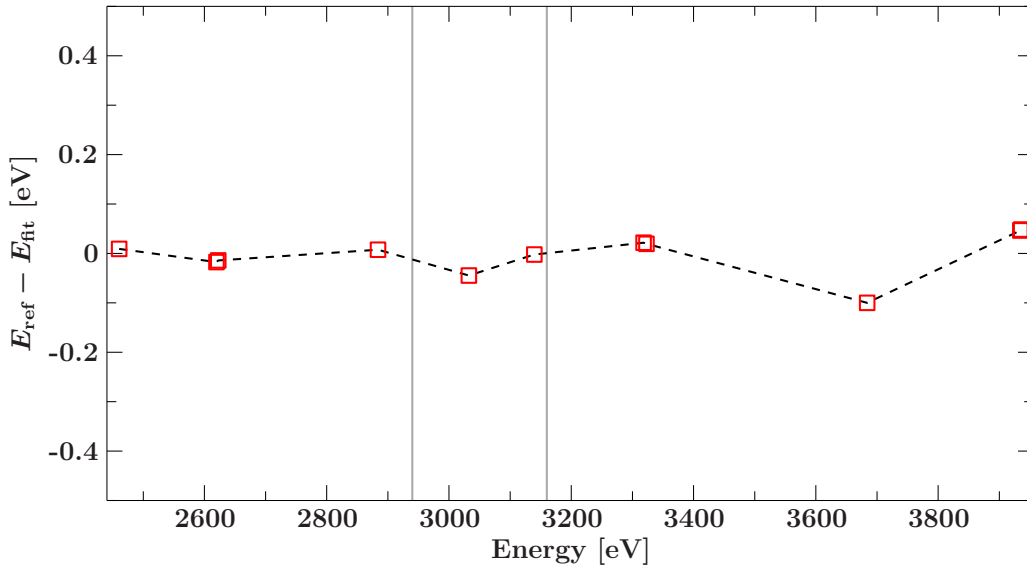
Figure 3.6: Quality of the calibration. Exemplified for the reference pixel. The energy range containing the argon spectra is indicated.

bin size of $0.5\,\mathrm{eV}$ is generated for each pixel. Finally, the histrograms are added up. The two resulting Ar spectra are shown in Fig. 3.7.

3.3.3 Resolution

Most of the major peaks in the spectra consist of several transistion lines, which blend with each other. In order to differentiate between at least some of them, the resolution of ECS has to be determined. For this purpose, a Gaussian function is fitted to a non blended transition line. Under the assumption that the resolution does not vary over the studied energy range, the full width at half maximum (FWHM) of that Gaussian can be identified with the detector's resolution. One line that meets that condition is the one originating in the transition from the state $^1\mathrm{P}_1$ to the ground state $^1\mathrm{S}$. Following the notation of Gabriel (1972), this transition is called the resonance line w. The fit function integrates a Gaussian function over every bin and assigns the resulting value to said bin. Hence, it is given by

$$g(E_{\mathrm{bin-lo}}, E_{\mathrm{bin-hi}}) = \frac{A}{\sigma\sqrt{2\pi}} \int_{E_{\mathrm{bin-lo}}}^{E_{\mathrm{bin-hi}}} \mathrm{d}E \exp\left[-\frac{(E-E_0)^2}{2\sigma^2}\right] \tag{3.1}$$

with fit parameters A, E_0, and σ. The relationship between the standard deviation σ and the FWHM is

$$\mathrm{FWHM} = 2\sqrt{2\ln 2}\,\sigma. \tag{3.2}$$

For the spectrum Ar1 the fit yields a standard deviation of $\sigma = 2.16 \pm 0.06\,\mathrm{eV}$, which corresponds to a FWHM of $5.09 \pm 0.15\,\mathrm{eV}$. For the second Ar spectrum, the parameters are $\sigma = 2.10 \pm 0.08\,\mathrm{eV}$ and consequently FWHM $= 4.95 \pm 0.19\,\mathrm{eV}$. Within their respective error bars these results match quite well. Their dimensions are also in line with the expectations for ECS (see Porter et al., 2008).

3.4 Comparison between the two Argon Spectra

In order to get a hang of the different lines in each peak, Gaussian functions (see equation 3.1) are fitted to the two spectra. Their standard deviations are frozen to the respective values determined in section 3.3.3. At the first step, only one Gaussian is assigned to every peak. Additionally, one has to mind the minima between the peaks, i.e., the spectrum's background. It results from transition lines that are too weak to be resolved. To address this point, a polynomial of second order is appended to the fit function. Since most of the spectral peaks result of more than one transition, the number of Gaussians is raised consecutively. At first, this is pretty easy and can be done by eye, but with
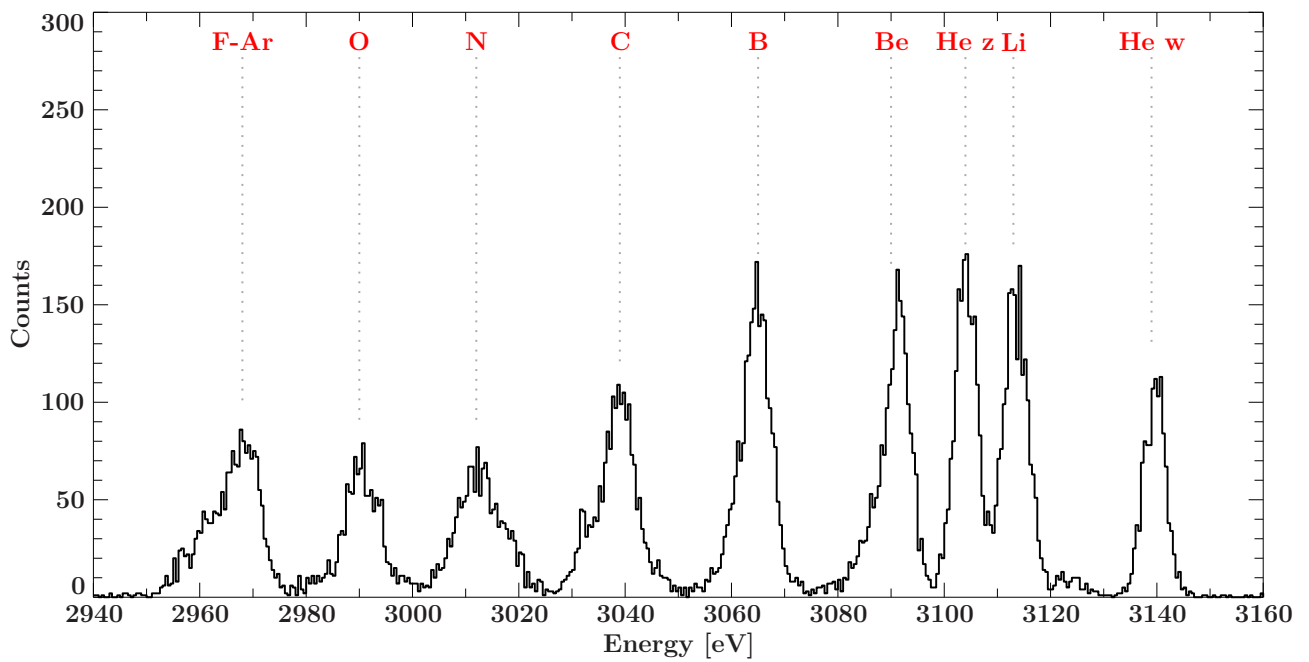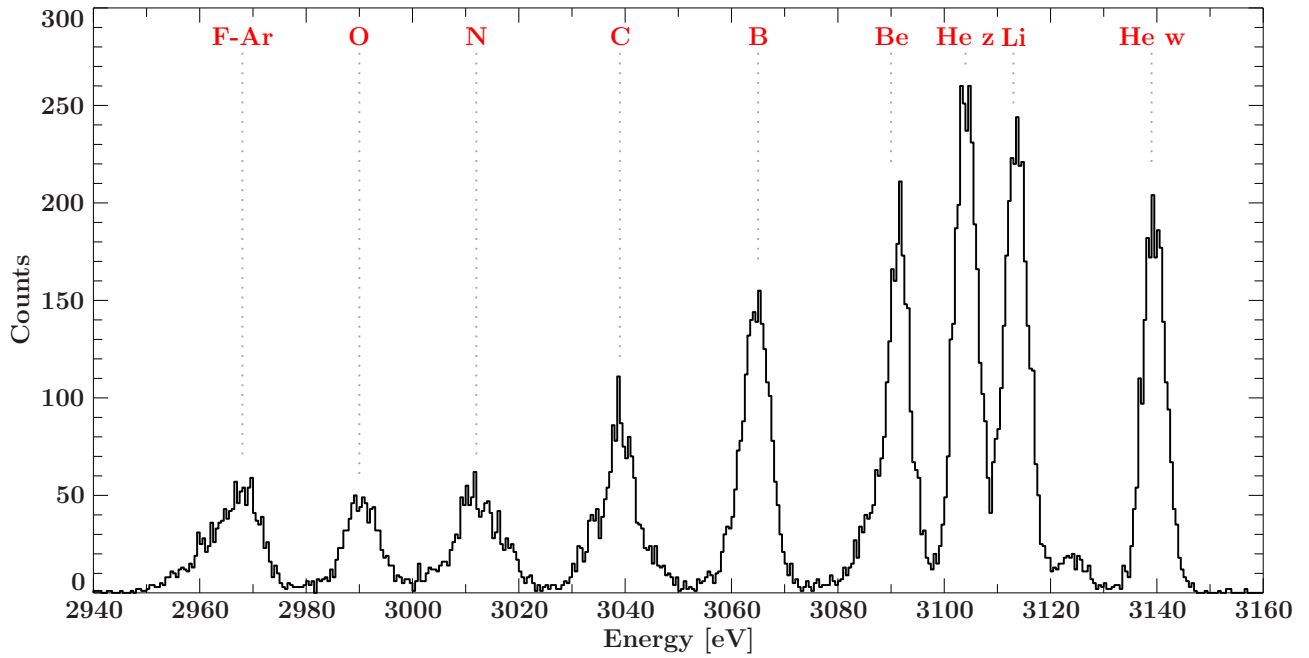
26

Figure 3.7: The two calibrated Ar spectra (top: Ar1, bottom: Ar2). Each peak is already marked with its principal charge state.

increasing number of Gaussian lines, the decision whether to add another component or not gets more and more difficult.

A Monte Carlo method included in the ISISscripts[4] is employed to cope with this issue. The simulation generates numerous fake spectra by using the spectral model without the component that needs to be tested for. In each bin of the applied energy grid, the number of counts is chosen randomly under the assumption of a Poisson distribution. The mean of this distribution is given by the corresponding value of the spectral model. Each resulting fake spectrum as well as the real one is fitted with the model containing the additional component and the one without it. The difference in chi square $\Delta\chi^2$ between the two fits is determined. The significance of the additional component is then given by the fraction of fake spectra whose $\Delta\chi^2$ is below the real one.

Following this procedure, a total amount of 20 Gaussians were distributed over the fit range from 2940 to 3160 eV in case of spectrum Ar1. For the second argon spectrum, the fit range was the same, but 22 single spectral components could be identified. The final fits for both spectra are shown in Fig. 3.8. The fact that the lower charge states are more pronounced in the second spectrum is visible to the naked eye. However, the question that is more intriguing is not about the abundances of the different ions, but rather how the spectral components change and whether any additional ones arise. This cannot be answered by just looking at the spectra. Therefore, the centers of the corresponding Gaussian functions describing the spectral components are regarded and compared with each other. They are listed in Table 3.2. For the better part, the line centers of the spectra match quite well within their respective error bars. Notable differences only occur in the N-like, the O-like, and the neutral (F- to Ar-like) peak. The low-energy tail of the N-like peak shows a distinct behaviour. Around 3005 eV a line center is found in the first spectrum, that cannot be detected in the second. As we will see in section 3.5, this is largely because a transition of Be-like ions is present in this region. Since the higher charge states are, as addressed above, more abundant in the first spectrum, said transistion line stands out visibly there. In comparison with the second spectrum, the remaining Gaussians have to be shifted to provide a constantly good fit. Consequently, the assignment of the transition lines to the Gaussians will show some variations (see section 3.5). In the O-like peak of the second spectrum, two additional components are found at 2998.7 eV and 2982.6 eV. In the first spectrum, the associated transition lines are too weak to be distinguishable from statistical fluctuations. The two components existing in both O-like peaks again agree exceptionally well. Just like in case of the N-like peak, it is the low-energy tail which sets the two neutral peaks slightly apart from each other.

3.5 Line Identification

In order to identify the fitted spectral components with their corresponding transition lines, we will make use of numerical calculations. This is necessary insofar as most of the fitted components are blends of numerous spectral lines lying too close together to be resolved separately. There exist various atomic codes for the calculation of all the atomic properties. In this thesis, the Flexible Atomic Code (FAC), written by Ming Feng Gu (2004), is used for that purpose.

3.5.1 The Flexible Atomic Code

FAC is a free-to-use software package[5] for the calculation of energy levels, radiative transition rates, the cross sections of electron impact excitation and ionization, photoionization, and autoionization. Most of the corresponding inverse processes are implemented as well. In order to find a basis of states, the orbitals are determined through a Dirac-Fock-Slater iteration. The latter is a self-consistent method, quite similar to the Hartree-Fock method described in section 2.3.2, but based on the Dirac equation and hence fully relativistic (Gu, 2004). In each iteration, the Dirac equation has to be solved for a certain potential. This is done by transforming the equation into a Schrödinger-like form and using Numerov's method to actually solve it (Gu, b). In the construction of the local central potential, which

---

[4]This is a set of ISIS functions and scripts provided by the Dr. Karl Remeis observatory in Bamberg, Germany. It is available for download at http://pulsar.sternwarte.uni-erlangen.de/hanke/science/X-ray/ISIS/isisscripts.html

[5]It is available at `http://sprg.ssl.berkeley.edu/labastro/`. The download includes a documentation of several unpublished papers and a manual.
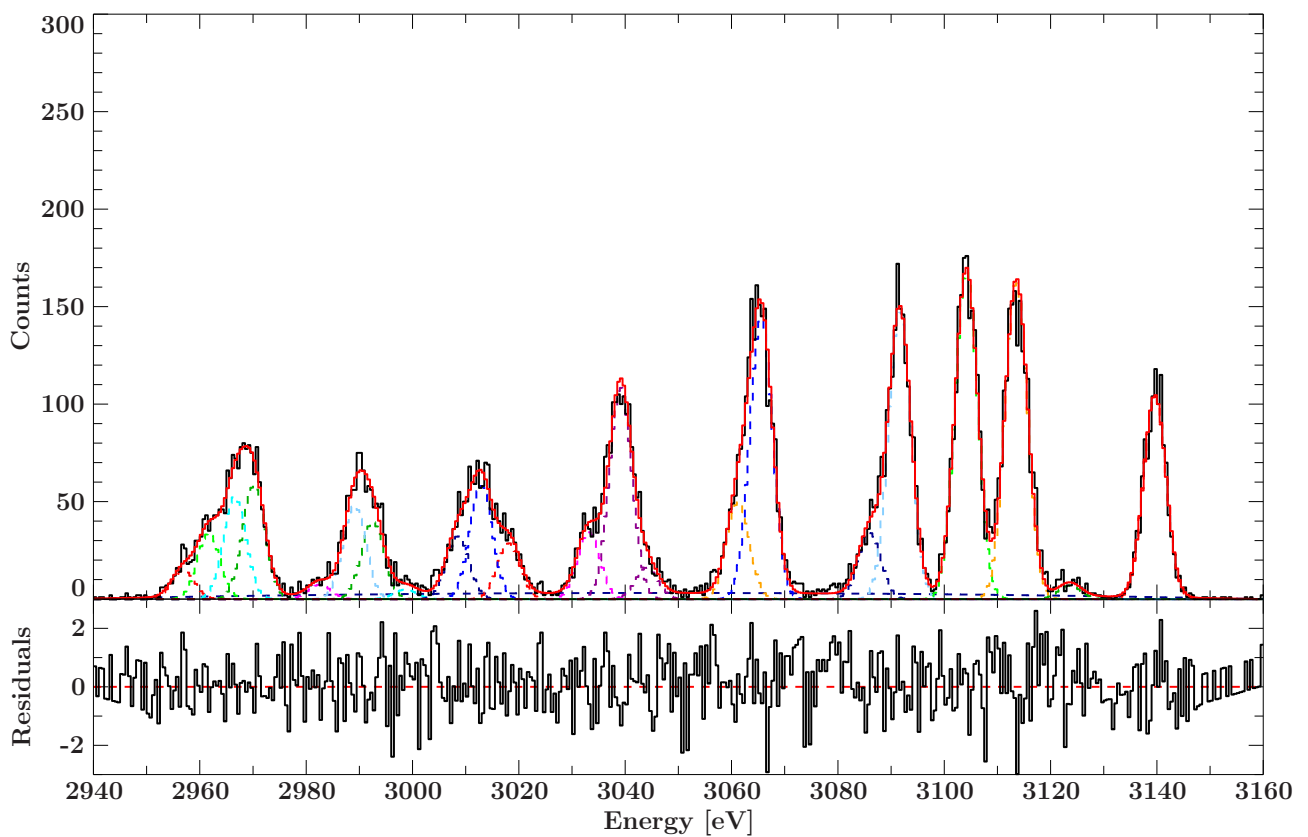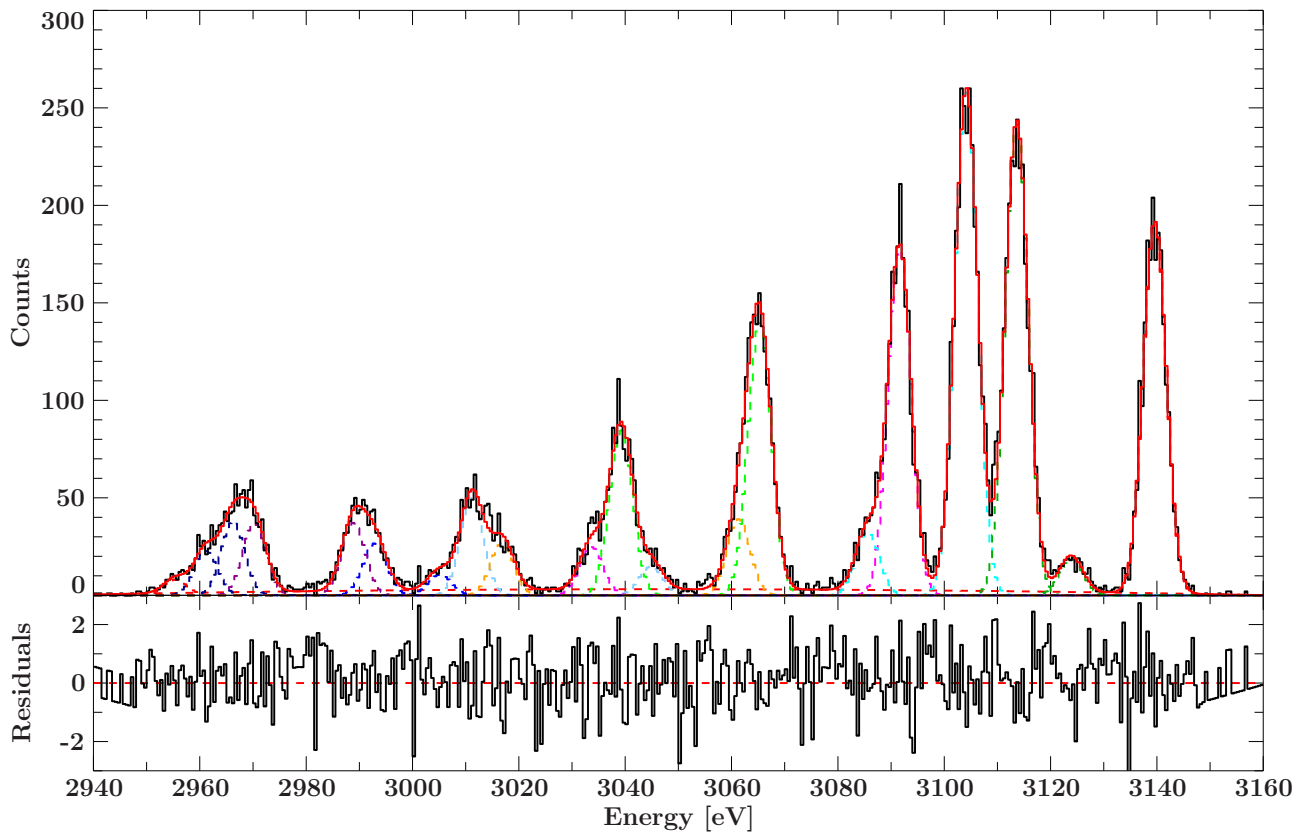
Figure 3.8: The two Ar spectra (top: Ar1, bottom: Ar2) with their single components and the resulting residuals. The data is shown in black, the total spectral model is displayed by the solid red line. The single components are illustrated by the dashed lines in random colors.

Table 3.2: Comparison between the two spectra. The fitted line centers of all the identified spectral components are assigned to the corresponding major peak.

Peak	Ar1 [eV]	Ar2 [eV]	Difference [eV]
He w	$3139.60^{+0.09}_{-0.08}$	$3139.60^{+0.12}_{-0.10}$	$0.00^{+0.14}_{-0.15}$
Li	$3123.8^{+0.4}_{-0.6}$	$3123.6^{+0.7}_{-0.9}$	0.2 ± 1.0
	$3113.63^{+0.07}_{-0.10}$	$3113.57^{+0.09}_{-0.14}$	$0.06^{+0.16}_{-0.14}$
He z	$3104.15^{+0.07}_{-0.09}$	$3104.17^{+0.09}_{-0.10}$	-0.02 ± 0.13
Be	$3091.60^{+0.10}_{-0.13}$	$3091.63^{+0.12}_{-0.14}$	-0.03 ± 0.18
	$3085.6^{+0.4}_{-0.5}$	$3086.0^{+0.4}_{-0.5}$	-0.4 ± 0.7
B	$3065.29^{+0.24}_{-0.20}$	$3065.58^{+0.16}_{-0.24}$	$-0.29^{+0.4}_{-0.26}$
	$3061.3^{+0.7}_{-0.6}$	$3061.3^{+0.4}_{-0.6}$	$0.0^{+1.0}_{-0.8}$
C	3044.8 ± 0.7	$3044.0^{+0.8}_{-1.5}$	$0.8^{+1.7}_{-1.1}$
	$3039.23^{+0.24}_{-0.23}$	$3039.14^{+0.20}_{-0.40}$	$0.1^{+0.5}_{-0.4}$
	3033.7 ± 0.5	3033.2 ± 0.4	0.5 ± 0.7
N	$3016.8^{+0.4}_{-0.6}$	3018.1 ± 0.5	$-1.3^{+0.7}_{-0.8}$
	3011.2 ± 0.4	$3012.9^{+0.5}_{-0.6}$	$-1.7^{+0.8}_{-0.7}$
	3005.2 ± 0.8	$3008.5^{+0.6}_{-0.7}$	-3.3 ± 1.1
O		$2998.7^{+1.2}_{-1.0}$	
	2992.9 ± 0.6	2992.5 ± 0.6	0.4 ± 0.9
	$2988.9^{+0.5}_{-0.6}$	$2989.1^{+0.5}_{-0.6}$	-0.2 ± 0.8
		2982.6 ± 0.9	
F-Ar	2970.3 ± 0.6	$2970.2^{+0.5}_{-0.4}$	0.1 ± 0.8
	$2966.2^{+0.9}_{-1.0}$	$2966.5^{+0.9}_{-0.8}$	$-0.3^{+1.3}_{-1.4}$
	$2961.1^{+0.9}_{-1.0}$	$2961.7^{+0.8}_{-0.7}$	$-0.6^{+1.2}_{-1.3}$
	$2955.4^{+0.9}_{-1.0}$	$2956.9^{+0.7}_{-0.6}$	$-1.5^{+1.1}_{-1.3}$

is involved in the later calculation of several physical processes, a fictitious averaged configuration can be used instead of a single configuration. Since the actual potential felt by the electrons depends on their configuration, the use of a single central potential leads to errors in the atomic structure. Therefore, an additional potential is calculated for every single configuration group. The difference of the obtained average energy values is then applied as a correction (Gu, a).

For the following computation of the radiative transition rates the single multipole approximation is used. Also, all the other quantities of excitation and ionization can be calculated once the energy levels are known. The accuracy with which the atomic structure can be stated amounts to a few eV for all other than H-like ions, while the transition rates and cross sections are usually accurate to $10 - 20\,\%$. In order to analyze the measured spectra, all the charge states from H-like to neutral argon were considered in the calculations with FAC. All in all, three different configuration groups were defined for each ionization state. The first one corresponds to the ground state, the second one has a hole in the K-shell, while the third one is missing an electron in the L-shell. In all the configuration groups, only the subshells belonging to $l = \mathrm{s}$ and $l = \mathrm{p}$ are allowed, given their accordance with the value of n. The rates for radiative transitions between and within the configuration groups were calculated. In addition, the cross sections for collisional excitation and ionization as well as the autoionization rates were computed. For the sake of completeness, the cross sections for photoionization and its reverse process, i.e., radiative recombination, were also calculated. With the collisional radiative model (crm) module, FAC provides a possibility to simulate the spectra of optically thin plasmas. In a first step, the data of the atomic states that should be included into the model are loaded. After that, the considered processes are taken into account and some additional parameters can be defined. In our case, the electron density and the energy distribution of the electron beam are specified. The former is set to $10^{12}\,\mathrm{cm}^{-3}$, while the latter is given by a Gaussian distribution with a width of $40\,\mathrm{eV}$. Lastly, the relative abundances of the different charge states are assigned. Since the initial conditions in the ion trap are not known (see below) they were chosen to be all equal. Having gathered the needed data, FAC employs an iterative linear equation solver to calculate the level population. In combination with the transition rates, this provides the total line emissivity.

However, the final calculation of the line emissivity is fraught with two major problems. First of all, the initial abundances in the trap are not known. Beyond that, FAC assumes the plasma to be in equilibrium. Through the cyclic dumping of the trap, that might actually never be the case in our experiment and we might have to deal with a transient plasma instead. Consequently, the calculation of the level population lacks consistency and has to be treated with caution. There is nothing to be done about these two issues, but since the main interest lies in the line energies of the strongest lines, this problem should not bother us too much, assuming that the line emissivities are at least rudimentally correct.

As a last point it has to be mentioned that, although the atomic data was calculated for all charge states, only H-like to Ne-like ions could be included into the simulation of the spectra. The addition of lower charge states to the model led to the level population having either physically unreliable solutions or not being solvable at all. Depending on the initial abundances, some lines showed implausibly high emissivities, the final abundances of various charge states had a negative value in equilibrium or the iteration of the level population did not converge.

3.5.2 The Kα-lines of Argon

After the FAC calculation, the lines with the highest emissivities are selected and respectively assigned to the Gaussian whose center is the closest to their transition energy. For all inspected lines, this identification is shown in Table 3.3. Here, the upper and lower levels of every transition are also denoted by the term symbols of jj coupling. In order to visualize the identification as well, the fitted spectra are shown together with the theoretically predicted lines in Fig. 3.9 and Fig. 3.10. The entire fit region is separated so that each panel shows one major peak of the spectrum. The fitted spectral components are labeled with the element symbol corresponding to the dominant charge state in that peak and, if necessary, with an additional number used to distinguish between them. In case of the He-like lines, the notation of Gabriel (1972) is adopted. These labels correspond to the ones used in Table 3.3. The FAC lines are plotted as colored vertical lines. Their emissivities are renormalized

separately in every panel so that the strongest line matches the maximum of the respective peak. Thereby, the ratio of the line emissivities lasts in each panel, but does not hold true for different ones. Most of the FAC lines match quite well to one of the fitted components. However, the assignment gets more difficult for the lower charge states. Here, some lines are so weak and blend so heavily that the identification is a bit arbitrary, especially, given the accuracy of the calculations with FAC for the transition energies. For the Gaussian labeled with F3, no strong lines are available. It results most likely through blends of lines which belong to the even lower charged ions, i.e., $N > 10$, that were not included into the plasma simulation. Yet, even if any atomic data was present for these ions, the identification would still be random, as mentioned above.

The limited accuracy of the calculations with FAC can best be observed on non blending lines. For instance, the He-like lines z (FAC: 3102.84 eV) and w (FAC: 3139.35 eV) show deviations of 1.32 eV and 0.25 eV in comparison to the measured line centers. Hence, especially line z has a fairly large offset. Nevertheless, both measured line centers agree exceptionally well with the well established reference values of (Drake, 1988, line z: 3104.14 eV, line w: 3139.58 eV).

Table 3.3: Identification of the fitted Gaussians with the strongest lines of the FAC simulation. The first column shows the respective charge state. Columns 2-4 display the data of the FAC lines, while columns 5 and 6 feature the labels (cf. figures 3.9 and 3.10) of the fitted spectral components and their averaged energies. Column 7 shows the difference between the transition energies calculated with FAC and the averaged energies of the measurement.

		jj coupling		Measurements		
Ion	FAC [eV]	lower level	upper level	Labels	Fit [eV]	Difference [eV]
Ne	2953.8	$1s^2 2s^2 2p^2_{1/2}((2p^3_{3/2})_{3/2}3p_{3/2})_0$	$(1s_{1/2}2s^2 2p^6 3p_{3/2})_1$	F4/F4	2956.2 ± 0.6	-2.4
Ne	2966.2	$1s^2 2s^2 (2p_{1/2}2p^4_{3/2}3p_{3/2})_1$	$(1s_{1/2}2s^2 2p^6 3p_{3/2})_1$	F2/F2	2966.4 ± 0.7	-0.2
Ne	2966.3	$1s^2 2s^2 (2p_{1/2}2p^4_{3/2}3p_{3/2})_2$	$(1s_{1/2}2s^2 2p^6 3p_{3/2})_1$			-0.1
Ne	2967.0	$1s^2 2s^2 (2p_{1/2}2p^4_{3/2}3p_{1/2})_1$	$(1s_{1/2}2s^2 2p^6 3p_{3/2})_1$			0.6
Ne	2967.2	$1s^2 2s^2 (2p_{1/2}2p^4_{3/2}3s_{1/2})_1$	$(1s_{1/2}2s^2 2p^6 3s_{1/2})_0$			0.8
Ne	2967.9	$1s^2 2s^2 2p^2_{1/2}((2p^3_{3/2})_{3/2}3p_{3/2})_2$	$(1s_{1/2}2s^2 2p^6 3p_{3/2})_1$			1.5
F	2968.2	$1s^2 2s^2 2p_{1/2}2p^4_{3/2}$	$(1s_{1/2}2s^2 2p^6)_{1/2}$			1.8
Ne	2968.6	$1s^2 2s^2 2p^2_{1/2}((2p^3_{3/2})_{3/2}3p_{1/2})_1$	$(1s_{1/2}2s^2 2p^6 3p_{3/2})_1$	F1/F1	2970.3 ± 0.4	-1.7
F	2970.4	$1s^2 2s^2 2p^2_{1/2}(2p^3_{3/2})_{3/2}$	$(1s_{1/2}2s^2 2p^6)_{1/2}$			0.1
O	2984.0	$1s^2 2s^2 2p^2_{1/2}(2p^2_{3/2})_0$	$(1s_{1/2}2s^2 2p^2_{1/2}(2p^3_{3/2})_{3/2})_1$	O2/O4	2985.8 ± 0.6	-1.8
O	2988.3	$1s^2 2s^2 (2p_{1/2}(2p^3_{3/2})_{3/2})_1$	$(1s_{1/2}2s^2 2p^2_{1/2}(2p^3_{3/2})_{3/2})_2$	O2/O3	$2989.0^{+0.4}_{-0.5}$	-0.7
O	2989.7	$1s^2 2s^2 2p^4_{3/2}$	$(1s_{1/2}2s^2 2p_{1/2}2p^4_{3/2})_1$			0.7
O	2990.1	$1s^2 2s^2 2p^2_{1/2}(2p^2_{3/2})_2$	$(1s_{1/2}2s^2 2p^2_{1/2}(2p^3_{3/2})_{3/2})_2$			1.1
O	2990.2	$1s^2 2s^2 (2p_{1/2}(2p^3_{3/2})_{3/2})_1$	$(1s_{1/2}2s^2 2p_{1/2}2p^4_{3/2})_1$			1.2
O	2991.5	$1s^2 2s^2 (2p_{1/2}(2p^3_{3/2})_{3/2})_1$	$(1s_{1/2}2s^2 2p_{1/2}2p^4_{3/2})_0$	O1/O2	2992.7 ± 0.5	-1.2
O	2991.9	$1s^2 2s^2 2p^2_{1/2}(2p^2_{3/2})_2$	$(1s_{1/2}2s^2 2p_{1/2}2p^4_{3/2})_1$			-0.8
O	2992.8	$1s^2 2s^2 (2p_{1/2}(2p^3_{3/2})_{3/2})_2$	$(1s_{1/2}2s^2 2p^2_{1/2}(2p^3_{3/2})_{3/2})_1$			0.1
Be	3000.5	$1s^2 (2p^2_{3/2})_2$	$(1s_{1/2}2s^2 2p_{3/2})_2$	N3/O1	$3002.0^{+0.8}_{-0.7}$	-1.5
Be	3004.2	$1s^2 (2p_{1/2}2p_{3/2})_2$	$(1s_{1/2}2s^2 2p_{3/2})_1$	N3/N3	3006.9 ± 0.6	-2.7
N	3007.1	$1s^2 2s^2 (2p^3_{3/2})_{3/2}$	$((1s_{1/2}2s^2 2p_{1/2})_1(2p^3_{3/2})_{3/2})_{5/2}$			0.2
N	3010.1	$1s^2 2s^2 (2p^3_{3/2})_{3/2}$	$((1s_{1/2}2s^2 2p_{1/2})_1(2p^3_{3/2})_{3/2})_{3/2}$	N2/N3	$3009.9^{+0.4}_{-0.5}$	0.2
N	3010.7	$1s^2 2s^2 (2p_{1/2}(2p^2_{3/2})_0)_{1/2}$	$((1s_{1/2}2s^2 2p_{1/2})_1(2p^3_{3/2})_{3/2})_{3/2}$	N2/N2	3012.1 ± 0.4	-1.4
N	3010.9	$1s^2 2s^2 (2p^3_{3/2})_{3/2}$	$((1s_{1/2}2s^2 2p_{1/2})_1(2p^3_{3/2})_{3/2})_{1/2}$			-1.2

Table 3.3 – continued from previous page

Ion	FAC [eV]	jj coupling		Measurements		
		lower level	upper level	Labels	Fit [eV]	Difference [eV]
N	3011.1	$1s^22s^2(2p_{1/2}(2p_{3/2}^2)_2)_{3/2}$	$(1s_{1/2}2s^22p_{1/2}^2(2p_{3/2}^2)_2)_{5/2}$			-1.0
N	3011.5	$1s^22s^2(2p_{1/2}(2p_{3/2}^2)_0)_{1/2}$	$((1s_{1/2}2s^22p_{1/2})_1(2p_{3/2}^3)_{3/2})_{1/2}$			-0.6
N	3013.1	$1s^22s^2(2p_{1/2}(2p_{3/2}^2)_2)_{3/2}$	$((1s_{1/2}2s^22p_{1/2})_0(2p_{3/2}^3)_{3/2})_{3/2}$			1.0
N	3013.6	$1s^22s^2(2p_{1/2}(2p_{3/2}^2)_2)_{5/2}$	$((1s_{1/2}2s^22p_{1/2})_1(2p_{3/2}^3)_{3/2})_{5/2}$			1.5
N	3013.8	$1s^22s^22p_{1/2}^22p_{3/2}$	$(1s_{1/2}2s^22p_{1/2}^2(2p_{3/2}^2)_2)_{3/2}$			1.7
N	3013.9	$1s^22s^2(2p_{1/2}(2p_{3/2}^2)_2)_{3/2}$	$(1s_{1/2}2s^22p_{1/2}^2(2p_{3/2}^2)_0)_{1/2}$			1.8
N	3016.4	$1s^22s^2(2p_{3/2}^3)_{3/2}$	$1s_{1/2}2s^22p_{3/2}^4$	N1/N1	3017.5 ± 0.4	-1.1
N	3016.5	$1s^22s^2(2p_{1/2}(2p_{3/2}^2)_2)_{5/2}$	$((1s_{1/2}2s^22p_{1/2})_1(2p_{3/2}^3)_{3/2})_{3/2}$			-1.0
N	3017.8	$1s^22s^22p_{1/2}^22p_{3/2}$	$((1s_{1/2}2s^22p_{1/2})_1(2p_{3/2}^3)_{3/2})_{1/2}$			0.3
C	3033.4	$1s^22s^2(2p_{3/2}^2)_2$	$((1s_{1/2}2s^22p_{1/2})_1(2p_{3/2}^2)_2)_3$	C3/C3	3033.5 ± 0.4	-0.1
C	3034.5	$1s^22s^2(2p_{3/2}^2)_0$	$(1s_{1/2}2s^2(2p_{3/2}^3)_{3/2})_1$			1.0
C	3034.8	$1s^22s^2(2p_{1/2}2p_{3/2})_1$	$((1s_{1/2}2s^22p_{1/2})_0(2p_{3/2}^2)_2)_2$			1.3
C	3036.1	$1s^22s^22p_{1/2}^2$	$(1s_{1/2}2s^22p_{1/2}^22p_{3/2})_1$			2.6
C	3037.79	$1s^22s^2(2p_{3/2}^2)_2$	$((1s_{1/2}2s^22p_{1/2})_1(2p_{3/2}^2)_2)_1$	C2/C2	$3039.19^{+0.16}_{-0.24}$	-1.40
C	3037.79	$1s^22s^2(2p_{1/2}2p_{3/2})_2$	$((1s_{1/2}2s^22p_{1/2})_1(2p_{3/2}^2)_2)_2$			-1.40
C	3039.27	$1s^22s^2(2p_{1/2}2p_{3/2})_1$	$((1s_{1/2}2s^22p_{1/2})_1(2p_{3/2}^2)_2)_1$			0.08
C	3039.52	$1s^22s^2(2p_{3/2}^2)_2$	$(1s_{1/2}2s^2(2p_{3/2}^3)_{3/2})_2$			0.33
C	3040.21	$1s^22s^2(2p_{3/2}^2)_2$	$((1s_{1/2}2s^22p_{1/2})_1(2p_{3/2}^2)_0)_1$			1.02
C	3040.49	$1s^22s^22p_{1/2}^2$	$((1s_{1/2}2s^22p_{1/2})_1(2p_{3/2}^2)_2)_1$			1.30
Li	3042.9	$1s^22p_{3/2}$	$1s_{1/2}2s^2$	C1/C1	$3044.4^{+0.6}_{-0.9}$	-1.5
C	3043.4	$1s^22s^2(2p_{1/2}2p_{3/2})_2$	$(1s_{1/2}2s^2(2p_{3/2}^3)_{3/2})_1$			-1.0
Li	3046.0	$1s^22p_{1/2}$	$1s_{1/2}2s^2$			1.6
B	3060.0	$1s^22s^22p_{3/2}$	$((1s_{1/2}2s^22p_{1/2})_12p_{3/2})_{5/2}$	B2/B2	3061.3 ± 0.5	-1.3
B	3061.9	$1s^22s^22p_{3/2}$	$((1s_{1/2}2s^22p_{1/2})_12p_{3/2})_{1/2}$			0.6
B	3062.7	$1s^22s^22p_{1/2}$	$((1s_{1/2}2s^22p_{1/2})_12p_{3/2})_{3/2}$			1.4
B	3064.66	$1s^22s^22p_{1/2}$	$((1s_{1/2}2s^22p_{1/2})_12p_{3/2})_{1/2}$	B1/B1	$3065.44^{+0.15}_{-0.16}$	-0.78
B	3065.03	$1s^22s^22p_{3/2}$	$(1s_{1/2}2s^2(2p_{3/2}^2)_2)_{3/2}$			-0.41
B	3067.82	$1s^22s^22p_{1/2}$	$(1s_{1/2}2s^2(2p_{3/2}^2)_2)_{3/2}$			2.38
B	3068.99	$1s^22s^22p_{3/2}$	$(1s_{1/2}2s^2(2p_{3/2}^2)_0)_{1/2}$			3.55

Table 3.3 – continued from previous page

| Ion | FAC [eV] | jj coupling | | Measurements | | Difference [eV] |
		lower level	upper level	Labels	Fit [eV]	
Be	3082.3	$1s^2(2s_{1/2}2p_{3/2})_2$	$(((1s_{1/2}2s_{1/2})_1 2p_{1/2})_{1/2}2p_{3/2})_1$	Be2/Be2	$3085.8^{+0.3}_{-0.4}$	-3.5
Be	3083.1	$1s^2(2s_{1/2}2p_{3/2})_2$	$(((1s_{1/2}2s_{1/2})_1 2p_{1/2})_{3/2}2p_{3/2})_3$			-2.7
Be	3085.2	$1s^2(2s_{1/2}2p_{3/2})_2$	$((1s_{1/2}2s_{1/2})_1(2p^2_{3/2})_2)_2$			-0.6
Be	3085.3	$1s^2(2s_{1/2}2p_{1/2})_0$	$(((1s_{1/2}2s_{1/2})_1 2p_{1/2})_{1/2}2p_{3/2})_1$			-0.5
Li	3086.4	$1s^2 2s_{1/2}$	$((1s_{1/2}2s_{1/2})_1 2p_{1/2})_{1/2}$			0.6
Li	3087.2	$1s^2 2s_{1/2}$	$((1s_{1/2}2s_{1/2})_1 2p_{1/2})_{3/2}$			1.4
Li	3089.36	$1s^2 2s_{1/2}$	$((1s_{1/2}2s_{1/2})_1 2p_{3/2})_{5/2}$	Be1/Be1	$3091.62^{+0.08}_{-0.10}$	-2.26
Be	3091.57	$1s^2 2s^2$	$(1s_{1/2}2s^2 2p_{3/2})_1$			-0.05
He	3102.84	$1s^2$	$(1s_{1/2}2s_{1/2})_1$	He z/He z	$3104.16^{+0.06}_{-0.07}$	-1.32
Li	3111.87	$1s^2 2s_{1/2}$	$((1s_{1/2}2s_{1/2})_0 2p_{1/2})_{1/2}$	Li2/Li2	$3113.60^{+0.06}_{-0.09}$	-1.73
Li	3113.59	$1s^2 2s_{1/2}$	$((1s_{1/2}2s_{1/2})_0 2p_{3/2})_{3/2}$			-0.01
He	3122.7	$1s^2$	$(1s_{1/2}2p_{1/2})_1$	Li1/Li1	$3123.7^{+0.5}_{-0.6}$	-1.0
Li	3124.6	$1s^2 2s_{1/2}$	$((1s_{1/2}2s_{1/2})_1 2p_{3/2})_{1/2}$			0.9
He	3125.4	$1s^2$	$(1s_{1/2}2p_{3/2})_2$			1.7
Li	3126.9	$1s^2 2p_{3/2}$	$(1s_{1/2}(2p^2_{3/2})_0)_{1/2}$			3.2
He	3139.35	$1s^2$	$(1s_{1/2}2p_{3/2})_1$	He w/He w	$3139.60^{+0.08}_{-0.07}$	-0.25
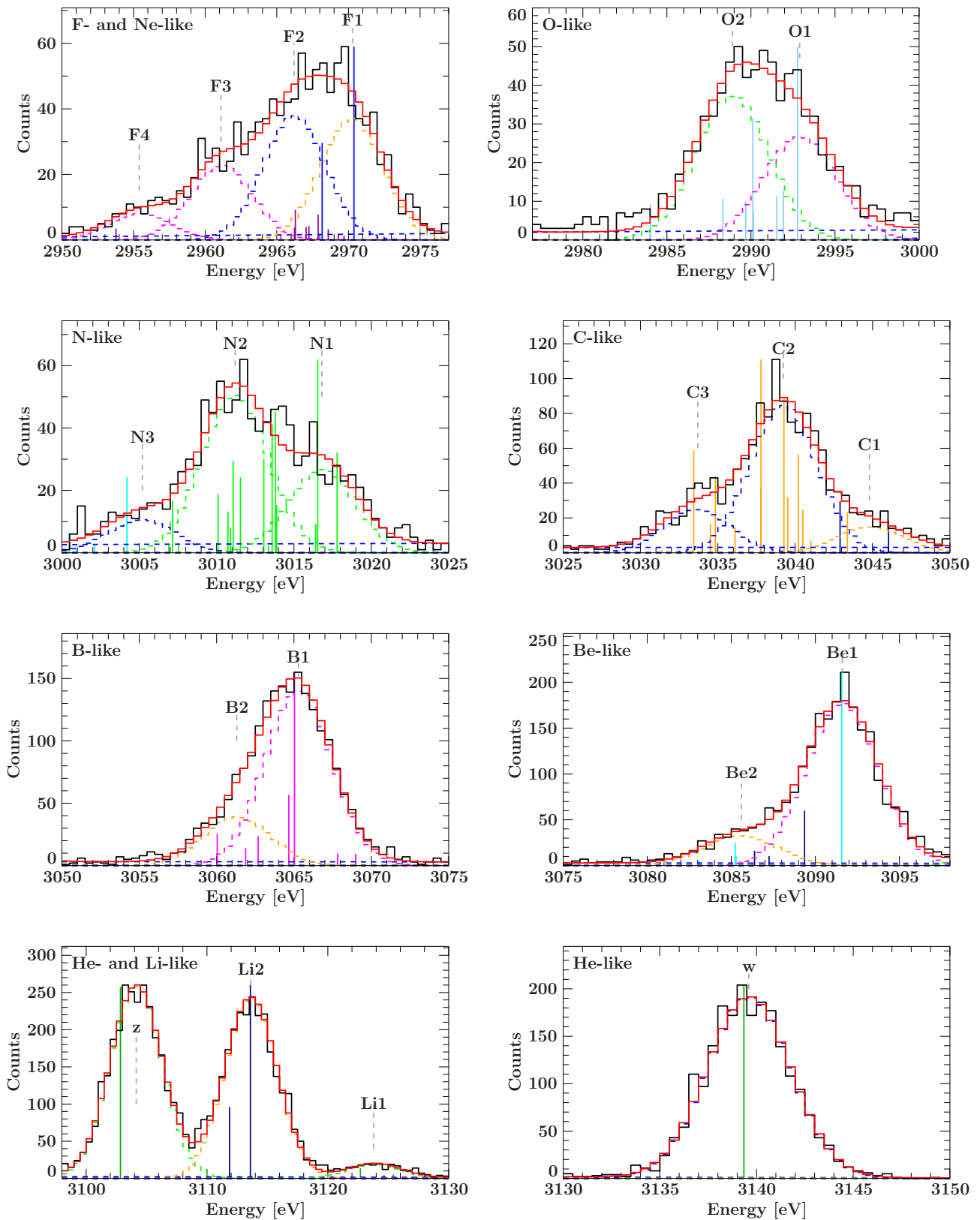
Figure 3.9: The fitted Ar1 spectrum. The data is shown in black, the total spectral model is displayed by the solid red line. The single components are illustrated by the dashed lines in random colors, the vertical lines signal the theoretical predictions of FAC.
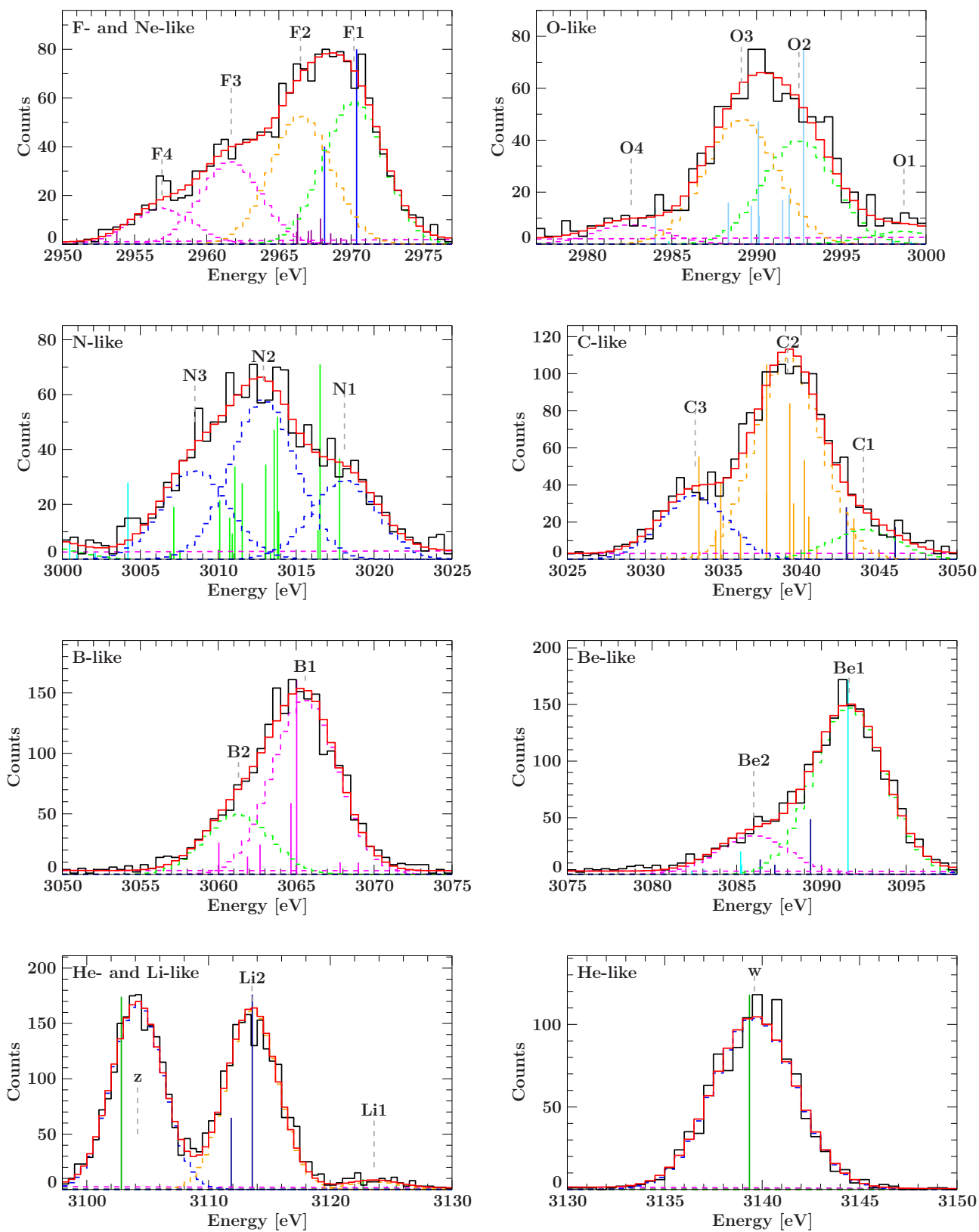
Figure 3.10: The fitted Ar2 spectrum, analog to figure 3.9.

Chapter 4

Conclusion

In this thesis the Kα-lines of ionized argon have been analyzed. The ions were produced, contained, and excited in an electron beam ion trap (EBIT) – strictly speaking the high energy variant SuperEBIT – at the Lawrence Livermore National Laboratory (LLNL). The resulting emission lines were recorded with the EBIT calorimeter spectrometer (ECS). In order to calibrate the detector, the H-like Lyman- and the He-like K-series of suitable elements were used due to their well known transition energies. In our case, calibration spectra of argon and sulfur have yielded the best result for the energy range of interest. After determining the detector's resolution, the calibrated spectra were fitted with correspondingly broad Gaussian lines. In addition, the plasma in the EBIT was simulated with the Flexible Atomic Code (FAC). The strongest lines of this simulation were then assigned to the fitted line centers. The theoretical energy values were compared with the ones coming from the measurement. For most lines, the difference was below two electron volts.

The identification of the measured line centers through the calculations with FAC are accompanied by two problems. On the one hand, the simulation does not reflect the actual situation. Because of the unknown initial charge balance in the ion trap, our ansatz is not self-consistent. Furthermore, neither the non-equilibrium state of the plasma – the ion trap is dumped time after time – nor all the possible charge states could be included to the FAC model. Consequently, the line emissivities show a certain amount of uncertainty. On the other hand, the accuracy of energy levels calculated with FAC lies in the area of a few electron volts. This might pose a problem for the unambiguity of the line identification as soon as heavily blending lines have to be assigned to the fitted spectral components. Regarding this issue, measurements with a crystal spectrometer could add clarity as the better resolution will make more lines resolvable. Bruhns (2005) presents such high-resolution measurements of the He-like and some of the Li-like transition lines of argon.

Bibliography

Beiersdorfer P., Beck B., Becker J.A., et al., 2003, AIP Conf. Proc. 652, 131

Beiersdorfer P., Bitter M., von Goeler S., Hill K.W., 1989, Phys. Rev. A 40, 150

Beiersdorfer P., Diaz F., Ishikawa Y., 2012, ApJ 745, 167

Bohr N., 1913, Phil. Mag. 26, 1

Boltzmann L., 1872, Wien. Ber. 66, 275

Bransden B., Joachain C., 2003, Physics of Atoms and Molecules, Prentice Hall, second edition

Bruhns H., 2005, Dissertation, Ruperto-Carola Universität Heidelberg

Dirac P., 1928, Proc. R. Soc. London, Ser. A 117, 610

Doppler C., 1842, Abh. d. königl. böhm. Ges. d. Wiss. 5, 465

Drake G.W., 1988, Can. J. Phys. 66, 586

Einstein A., 1917, Phys. Z. 18, 121

Fraunhofer J.v., 1814, Denkschriften der Königlichen Akademie der Wissenschaften zu München 5, 193

Gabriel A.H., 1972, MNRAS 160, 99

Garcia J.D., Mack J.E., 1965, J. Opt. Soc. Am. 55, 654

Gibbs J., 1902, Elementary Principles in Statistical Mechanics, C. Scribner's sons

Gu M.F., , FAC 1.1.1 Manual

Gu M.F., , The Flexible Atomic Code: I. Atomic Structure

Gu M.F., 2004, AIP Conf. Proc. 730, 127

Hell N., 2012, Masterarbeit, Friedrich-Alexander-Universität Erlangen-Nürnberg

Houck J.C., Denicola L.A., 2000, In: Manset N., Veillet C., Crabtree D. (eds.) Astronomical Data Analysis Software and Systems IX. Astron. Soc. Pacific, Conf. Ser. 216, p. 591

Johnson W.R., Soff G., 1985, Atomic Data Nucl. Data Tables 33, 405

Kirchhoff G., 1860, Ann. Phys. 185, 148

Kirchhoff G., Bunsen R., 1861, Ann. Phys. 189, 337

Lamb W., Retherford R., 1947, Phys. Rev. 72, 241

Levine M.A., Marrs R.E., Bardsley J.N., et al., 1989, Nucl. Instrum. Methods Phys. Res., Sect. B 43, 431

Levine M.A., Marrs R.E., Henderson J.R., et al., 1988, Phys. Scr. Vol. T 22, 157

Marrs R.E., 2008, Can. J. Phys. 86, 11

McCammon D., 2005, Thermal Equilibrium Calorimeters - An Introduction, p.1, Berlin, Heidelberg: Springer

Pauli W., 1925, Z. Physik 31, 765

Pauli W., 1926, Z. Physik 36, 336

Pauli W., 1927, Z. Physik 43, 601

Planck M., 1900, Verhandl. der Deutschen Physikalischen Gesellsch. 2, 202

Poole, C.P. J., Farach H., 1982, Found. Phys. 12, 719

Porter F.S., Gygax J., Kelley R.L., et al., 2008, Rev. Sci. Instrum. 79, 307

Ritz W., 1909, J. Reine Angew. Math. 135, 1

Shankar R., 1994, Principles of Quantum Mechanics, Springer, second edition

Stark J., 1913, Naturwissenschaften 1, 1182

Vainshtein L.A., Safronova U.I., 1985, Phys. Scr. 31, 519

Zeeman P., 1897, ApJ 5, 332

Acknowledgements

Erklärung

Hiermit versichere ich, dass ich die vorliegende Arbeit selbstständig verfasst und keine anderen als die angegebenen Quellen und Hilfsmittel benutzt habe, dass alle Stellen der Arbeit, die wörtlich oder sinngemäß aus anderen Quellen übernommen wurden, als solche kenntlich gemacht sind und dass die Arbeit in gleicher oder ähnlicher Form noch keiner anderen Prüfungsbehörde vorgelegt wurde.

Nürnberg, den 3. September 2013

. . . .
Andreas Wolf